Planetary and Space Science 195 (2021) 105136

Contents lists available at ScienceDirect

Planetary and Space Science

journal homepage: www.elsevier.com/locate/pss

Lermontov crater on Mercury: Geology, morphology and spectral properties of the coexisting hollows and pyroclastic deposits

M. Pajola [a,*], A. Lucchetti [a], A. Semenzato [b], G. Poggiali [c,d], G. Munaretto [a,e], V. Galluzzi [f], G.A. Marzo [g], G. Cremonese [a], J.R. Brucato [c], P. Palumbo [h,f], M. Massironi [i]

[a] INAF-Astronomical Observatory of Padova, Vicolo Dell'Osservatorio 5, 35122, Padova, Italy
[b] Engineering Ingegneria Informatica S.p.A., Venezia, Italy
[c] INAF-Astrophysical Observatory of Arcetri, Firenze, Italy
[d] Università Degli Studi di Firenze, Firenze, Italy
[e] Department of Physics and Astronomy "G. Galilei", Università di Padova, Padova, Italy
[f] INAF-Institute for Space Astrophysics and Planetology, Roma, Italy
[g] ENEA C. R. Casaccia, Roma, Italy
[h] DiST-Università Degli Studi di Napoli "Parthenope", Napoli, Italy
[i] Geosciences Department, University of Padova, Padova, Italy

A B S T R A C T

We present a multidisciplinary analysis of Lermontov crater, located at 15.24°N, −48.94°E in the Kuiper quadrangle of Mercury. By means of MESSENGER multiband MDIS-WAC and monochrome MDIS-NAC images, we prepare a high-resolution geological map of the crater and its closest surroundings, highlighting the presence of coexisting hollows and pyroclastic deposits on its floor. On the photometrically corrected MDIS-WAC multiband dataset, we apply an unsupervised clustering technique that spectrally separates the different materials located both inside and outside Lermontov crater. We observe that the pyroclastic deposits located on the crater's floor have a steep, red spectral behaviour dominated by the presence of a mixture of various pyroxenes containing Ti and Ni. On the contrary, the vents' rims are characterised by several hollows whose spectral slope is bluer than that of the pyroclastic deposits. By comparing the vent hollows to the hollows located farther out on the crater floor, we observe a steeper 0.62–0.82 μm spectral trend for those within the vents. The vent hollows' spectrum is more similar to the pyroclastic one in the above mentioned wavelength range. In addition, the vent hollows 0.55 μm absorption band could be related to CaS, while the small differences in slope at 0.48 μm and 0.62 μm could be due to the presence of other volatiles compounds, such as MgS or chlorides. When compared to hollows located in other hermean geological settings, Lermontov hollows are characterised by steeper spectra. This supports the interpretation that when hollows form, their bright deposits do not completely overwrite the spectral signature of the surrounding terrain, and their spectroscopic appearance is mixed with the composition of the terrain where they form.

1. Introduction

Lermontov is a 166 km-wide crater located at 15.24°N, −48.94°E in the Kuiper quadrangle (−22° to +22° lat., 0° to −72°E long.) of Mercury (Fig. 1A). This crater was first identified in Mariner 10 images (DeHon et al., 1981) thanks to its particularly bright floor characterised by smooth plains (Fig. 1B). A first possible explanation for this brightness behaviour was given by Dzurisin (1977), who suggested that it might be the direct result of fumarolic alteration along multiple fractures located on the floor. Instead, Rava and Hapke (1987) noted how the crater floor appears to have a lower crater density than the surroundings. This aspect, coupled with the occurrence of irregular rimless pits in its northeast sector, was considered indicative of endogenic modification (Schultz, 1977). Rava and Hapke (1987) then proposed that Lermontov's bright interior might have been emplaced by pyroclastic activity, i.e. volcanic eruptions caused by the fragmentation and upward propulsion of magma particles driven by the expansion of volatile species released from rising bodies of magma (Wilson and Head, 1981).

Using MESSENGER (MErcury Surface, Space, ENvironment, GEochemistry, and Ranging; Solomon et al., 2007) flybys 1–3 MDIS (Mercury Dual Imaging System; Hawkins et al., 2007) images, Kerber et al. (2011) identified two pyroclastic deposits and their vents on the floor of Lermontov: a smaller vent located toward the north-east that has crisp edges (Goudge et al., 2014), and a larger vent with much more degraded edges situated in the south-west (Fig. 1C; Goudge et al., 2014). In particular, Kerber et al. (2011) suggested that the vent associated with the Lermontov NE pyroclastic deposit is morphologically similar to the vent associated with the lunar pyroclastic deposit Sulpicius Gallus

* Corresponding author.
E-mail address: maurizio.pajola@inaf.it (M. Pajola).

https://doi.org/10.1016/j.pss.2020.105136
Received 29 April 2020; Received in revised form 23 October 2020; Accepted 9 November 2020
Available online 11 November 2020

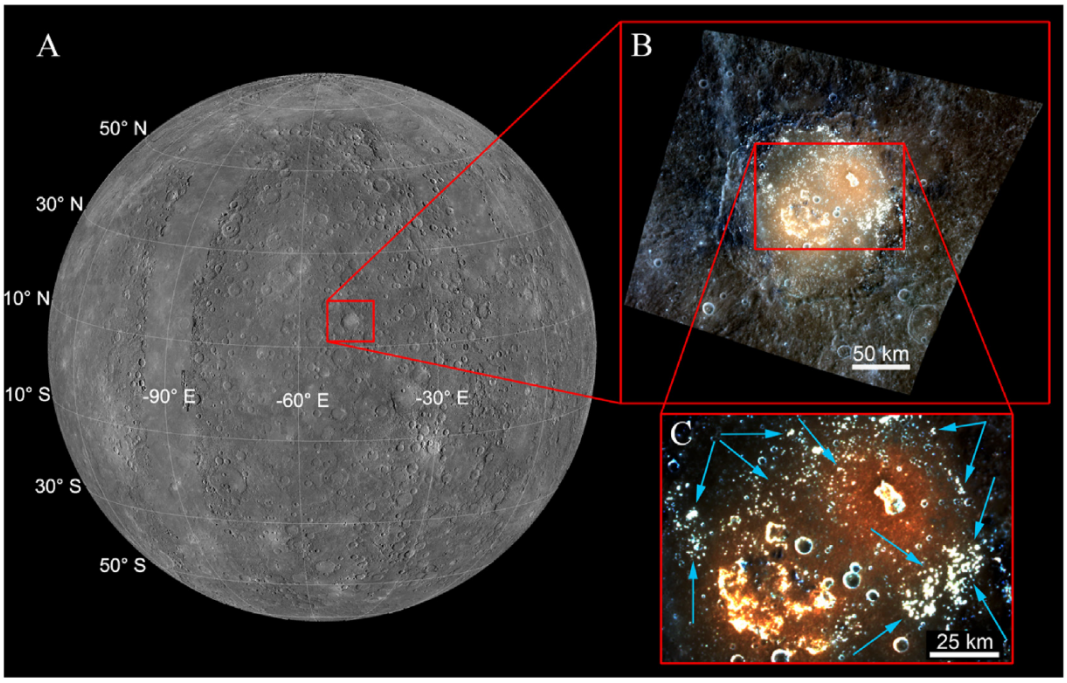

Fig. 1. A) Context image of Mercury with the location of Lermontov crater (red square). B) MESSENGER MDIS-WAC RGB image of Lermontov (the red channel of the RGB is the 0.947 ***μm*** filter, the green channel is the 0.628 ***μm*** filter while for the blue channel we used the 0.433 ***μm*** filter). C) Stretched RGB closeup showing the red pyroclastic deposits and the location (light blue arrows) of the hollows. (For interpretation of the references to colour in this figure legend, the reader is referred to the Web version of this article.)

(Lucchitta and Schmitt, 1974; Gaddis et al., 2003), where a non-circular shape, rimless margins and lack of ejecta deposits is evident, but the Lermontov vent is twice as large as the vent at Sulpicius Gallus.

Pyroclastic deposits on Mercury generally appear to be brighter and redder than the global average, i.e. they show both higher reflectance than background terrain and a more steeply inclined visible to infrared (Vis NIR) reflectance slope (Robinson et al., 2008; Blewett et al., 2009, Kerber et al., 2009). This is the case for Lermontov's deposits (Fig. 1C), which are classified in the Vis NIR range as "red" (Izenberg et al., 2014). The Lermontov crater floor is also of extreme interest because it hosts abundant hollows (Blewett et al., 2013), which are shallow, irregular and rimless flat-floored depressions with bright interiors and halos (Blewett et al., 2011, 2016), generally exhibiting a bluer spectral trend (Vilas et al., 2016). The collocation of bright, blue hollows and bright, red pyroclastic material was found in several other craters on the surface of Mercury, such as Praxiteles, Tyagarja and Scarlatti (Blewett et al., 2011; Kerber et al., 2011). The analysis of these sites would suggest that, as the hollows are hosted in the dark low-reflectance-material which partially covers those craters, the low-reflectance-material substrate may be buried under a thin mantle of pyroclastic deposits (Blewett et al., 2013).

Moreover, given that pyroclastic material and hollows are both the results of volatile-driven processes, their coexistence is of pivotal importance to provide information about Mercury's surface, subsurface structure and composition (Denevi et al., 2018a).

The presence of both pyroclastic deposits and hollows in Lermontov provides an opportunity to compare both spectral trends and to study their mutual mineralogies and uniquenesses. In addition, Lermontov's hollows, which are located on pyroclastic deposits, can be compared with hollows elsewhere on Mercury in completely different geological settings (Lucchetti et al., 2018).

The aim of this work is therefore to provide a detailed geological overview of the Lermontov crater. In addition, we focus on the red pyroclastic deposits estimating both the possible volatile quantities that may have triggered the vent explosions, as well as their mineralogical composition. We then study the hollows spectrophotometric behaviour comparing their mineralogy with the pyroclastic deposits where they formed. Finally, the differences of these hollows with those unrelated to pyroclastic activity are presented.

2. Material and methods

2.1. Imagery and DTM for geological mapping

In order to prepare the geological map of Lermontov crater and its closest surroundings, we first imported the monochromatic MDIS Basemap Data Record (BDR; spatial scale of ~166 m/pixel, Fig. 2A, see Supplementary Material Table 1 for all basemaps used) into the Environmental Systems Research Institute ArcGIS 10.5 software (hereafter ArcGIS). The MDIS BDR is a global map of the radiance factor, I/F, measured by the NAC (Narrow-Angle Camera) and the WAC (Wide-Angle Camera; Hawkins et al., 2007) filter no. 7 (both centred at 0.749 μm) at moderate/high incidence angles, and then photometrically normalised to a solar incidence angle of 30°, an emission angle of 0°, and a phase angle of 30°, with a spatial sampling of 256 pixels per degree.

To be able to map small features such as hollows located on the crater's floor, we also processed several MDIS-NAC frames into eight different mosaics covering much of Lermontov crater using the U.S. Geological Survey (USGS) Integrated Software for Imagers and Spectrometers (ISIS3) software (see Supplementary Material Table 2). The resulting spatial scales of these mosaics range between 26 m/pixel and 48 m/pixel (Fig. 2B).

Considering the coordinate range of the Lermontov crater (i.e. low latitudes), in order to minimise distortions inside the mapping area we adopted an Equidistant Cylindrical projection (see Davies et al., 1978) centred at 15.2°N, −48.9°E, with a sphere of radius 2439.4 km (Denevi et al., 2018b) for all images presented in this work, including full-crater views and close-ups.

We then downloaded the low-resolution MD3-colour global mosaic (Fig. 3A), as well as the enhanced-colour basemap (both obtained from MDIS and with a scale of ~665 m/pixel; Fig. 3B). On the two colour datasets, we applied the Image Sharpening Transformation technique (Colour Normalised (Brovey) Sharpening; Thomas et al., 2014; Du et al.,

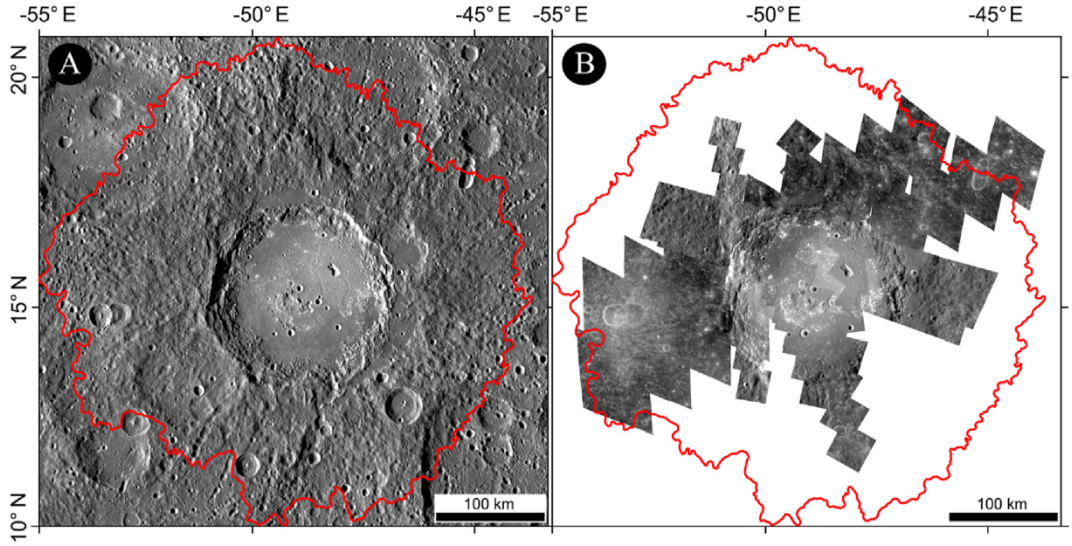

Fig. 2. A) The MDIS BDR dataset (~166 m/pixel) covering the Lermontov crater study area. B) The MDIS NAC mosaics (26–48 m/pixel) prepared for the high-resolution geological mapping. The red line shows the extent of Lermontov ejecta in both panels. (For interpretation of the references to colour in this figure legend, the reader is referred to the Web version of this article.)

2007; Parente and Pepe, 2017) obtaining the enhancement of their spatial resolution up to the level of the monochrome basemap, but maintaining the colour information (Fig. 3C and D). To complement this multiband dataset, we used the monochrome high-incidence angle and the low-incidence angle MDIS mosaics (both with a scale of ~166 m/pixel; Fig. 4A and B) mapping the geological units by highlighting both "colours" and different textures, at an average scale of ~1:400 000.

We also took into account the USGS stereo-derived digital terrain

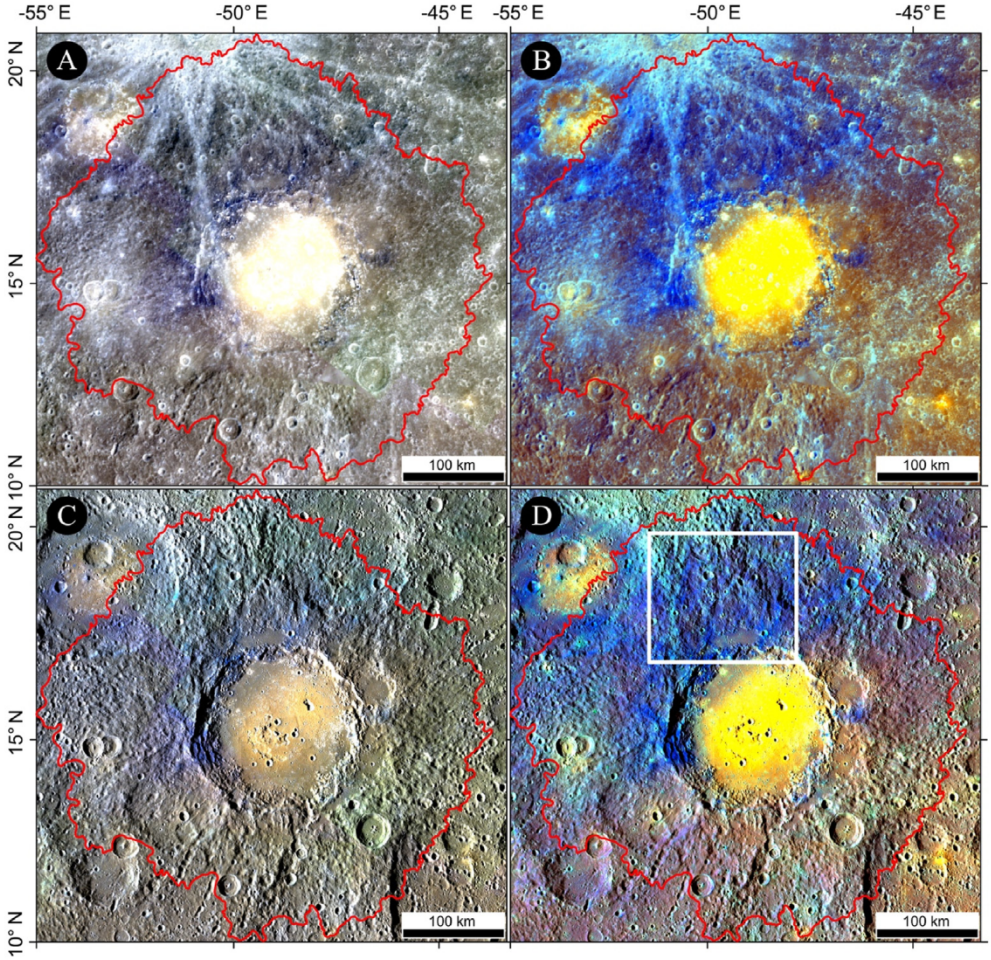

Fig. 3. The Lermontov crater, whose ejecta extent is represented by the red line in each figure panel. A) MD3-colour global mosaic (665 m/pixel), obtained by using the 0.996 μm, 0.749 μm and 0.433 μm narrow-band filters in the red, green and blue channels of the RGB, respectively. B) The MDIS enhanced-colour basemap of Lermontov (665 m/pixel), obtained by using the second principal component, the first principal component, and the 0.433 μm/0.996 μm ratio in the red, green and blue channels, respectively. C) Colour Normalised Brovey Sharpening of panel A (166 m/pixel). D) Colour Normalised Brovey Sharpening of panel B (166 m/pixel). The white box shows the extent of Fig. 7A. (For interpretation of the references to colour in this figure legend, the reader is referred to the Web version of this article.)

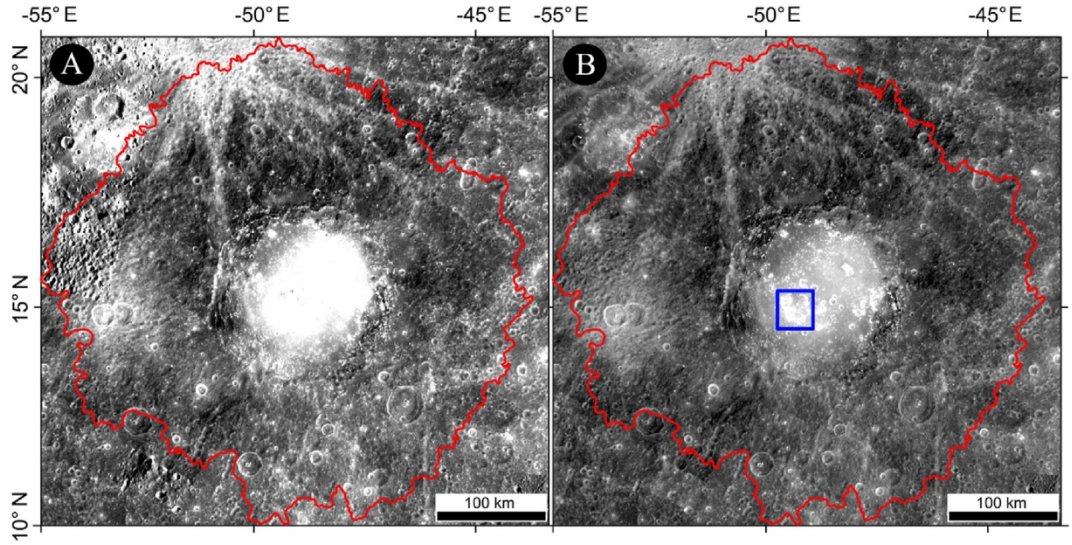

Fig. 4. A) The MDIS high-incidence angle mosaic (scale of ~166 m/pixel) covering the Lermontov crater study area. B) The low-incidence angle mosaic (scale of ~166 m/pixel). Both images are used to highlight the different textures of the geological units. The blue box shows the extent of Fig. 6A. On both panels the red line shows the extent of Lermontov ejecta. (For interpretation of the references to colour in this figure legend, the reader is referred to the Web version of this article.)

model (DTM v2, with sampling of 665 m/pixel; Becker et al., 2016) of the area, which was used for a thorough interpretation of the surrounding surface morphology (Fig. 5).

Thanks to the spatial scale provided by the NAC images available for Lermontov's floor, all hollows were mapped at a scale between 1:60 000 and 1:100 000. In the north-eastern part of the crater, hollow identification was aided by the 155 m scale DTM (Fig. 5) published by Fassett (2016). We followed the USGS digital cartographic standard (https://ngmdb.usgs.gov/fgdc_gds/geolsymstd.php) for map symbolisation (Figs. 6 and 7).

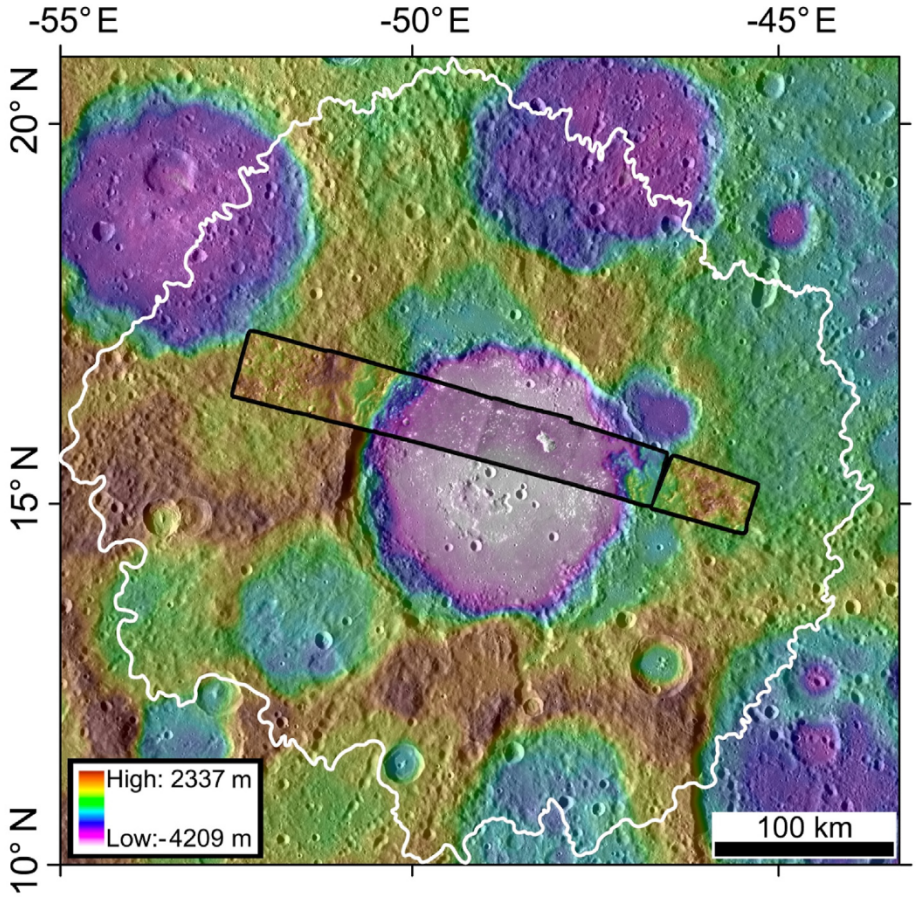

Fig. 5. The USGS stereo-derived digital terrain model (spatial sampling of 665 m/pixel; Becker et al., 2016) covering the Lermontov study area. The white line shows the extent of Lermontov ejecta. The black line shows the 155 m scale DTM prepared by Fassett (2016).

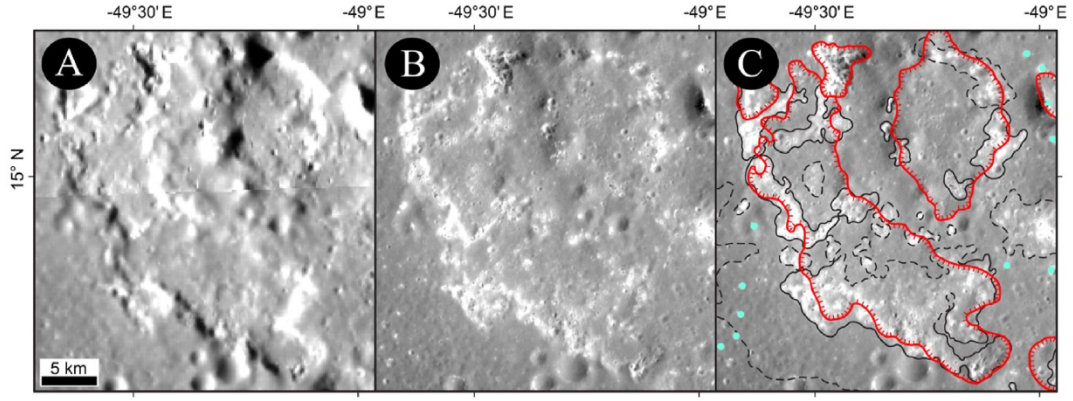

Fig. 6. Close-up displaying hollow clusters and volcanic pits located in the south-west portion of Lermontov's floor (the location is in Fig. 4B). A) MDIS BDR. B) High-resolution NAC Mosaic no. 1. C) Same as B) but with geologic contacts, linear and point features. The solid lines represent certain contacts, while dashed lines represent approximate contacts. Red lines with ticks represent volcanic pit crests (ticks point into the pit), which are better identified in A) (although with lower resolution, the BDR displays better topographic information in this area with respect to the NAC mosaic). Light blue dots identify isolated hollows that are too small to be mapped as polygons (i.e. geologic units), but sufficiently well-resolved to be identified. (For interpretation of the references to colour in this figure legend, the reader is referred to the Web version of this article.)

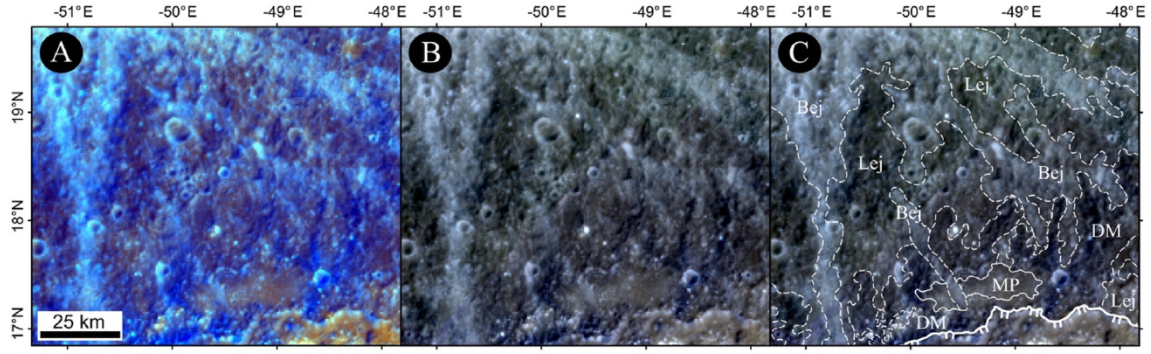

Fig. 7. Global mosaic close-up situated north of Lermontov crater (the location is in Fig. 3D). A) MDIS enhanced-colour; B) MDIS MD3-colour global mosaic; C) Same as B) but with geologic contacts displaying the overlapping relations between Lermontov crater ejecta (Lej), Bark crater ejecta (Bej – with brighter colour), dark material (DM) and melt pool (MP), respectively excavated and produced by the Lermontov impact. Solid white lines represent certain contacts, while dashed white lines represent approximate contacts. The Lermontov crater rim is identified by a solid white line with ticks toward the inner wall scarp. For the geologic units associated with these contacts the reader is referred to the main geologic map (Fig. 10). (For interpretation of the references to colour in this figure legend, the reader is referred to the Web version of this article.)

2.2. Spectrophotometry and clustering

To perform the spectrophotometric analysis for the Lermontov pyroclastic deposits, hollows and their closest surroundings we used MDIS-WAC images. This multispectral dataset has a spatial scale of 266 m/pixel through 11 filters (0.433, 0.480, 0.559, 0.629, 0.699, 0.749, 0.828, 0.899, 0.947, 0.996 and 1.103 μm, see Supplementary Material Table 3). As done by Lucchetti et al. (2018), all images were photometrically corrected to the standard viewing geometry (i.e. incidence angle of 30°, emission angle of 0° and phase angle of 30°) using the Hapke model with parameters derived in Domingue et al. (2015). This was accomplished through the ISIS3 image processing package of the USGS (https://isis.astrogeology.usgs.gov/). Once the unnormalised photometrically corrected data set was obtained, we then focused on four different selections (Fig. 8), three with dimensions of 150 × 150 pixels, all located inside the crater's floor. Such selections were chosen in order to make comparisons between the different pyroclastic deposits, vents and the hollows. Selection no.1, called Sel. 1, is located on the SW pyroclastic deposit, Sel. 2 is located on the NE pyroclastic deposit and vent, Sel. 3 lies on the hollow cluster situated in the central-east side of the floor. In addition, we added another selection, Selection no. 4, called Sel. 4, on the ejecta deposits (100 × 100 pixels) in order to make a comparison with an area not covered by pyroclastic deposits. On such MDIS multiband selections we then applied a statistical clustering based on a K-means algorithm developed and evaluated by Marzo et al. (2006). This algorithm makes use of the Calinski-Harabasz criterion (Calinski and Harabasz, 1974) to find the intrinsic number of clusters, making the process unsupervised. Each resulting cluster is characterised by its average spectrum and associated standard deviation. In addition, the relative geographical information of each spectrum is maintained in the process, and the resulting clusters can be located on the map. Therefore, correlations between spectral trends and geographical features can be investigated. This technique has been extensively validated using spectral datasets and applied to Mars (Marzo et al. 2006, 2008, 2009; Fonti and Marzo 2010), Iapetus (Pinilla-Alonso et al., 2011; Dalle Ore et al., 2012), Phobos (Pajola et al., 2018), Charon (Dalle Ore et al., 2018) and Mercury (Lucchetti et al., 2018). Since the Marzo et al. (2006) algorithm is agnostic of the physical and/or mineralogical meaning of the resulting clusters a subsequent scientific interpretation is then required.

3. Mineralogy

In order to identify the possible mineralogical composition of the different spectral clusters obtained, we performed a spectral matching with the data derived from the RELAB catalogue of the Brown University (http://www.planetary.brown.edu/relab/).

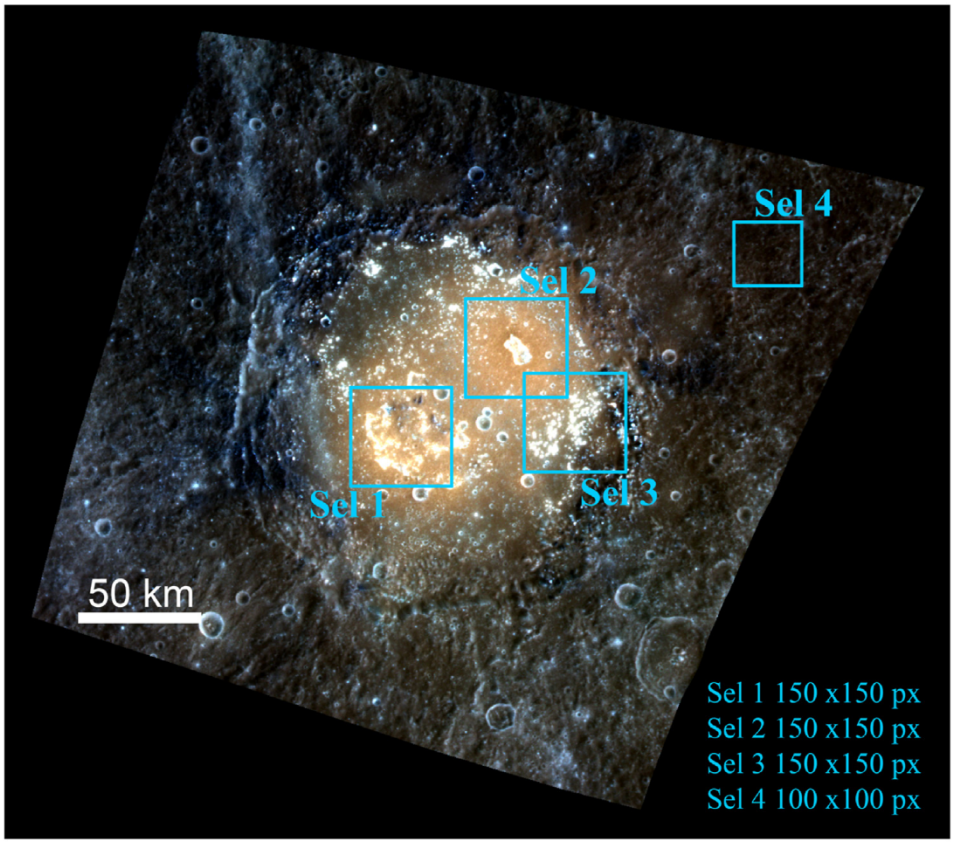

Fig. 8. The four selected areas where we applied the spectral clustering technique. Three (Sel. 1, 2 and 3) are located inside Lermontov crater's floor, while one (Sel. 4), is located well outside the crater's rim inside the ejecta deposits.

To date, few laboratory measurements have been obtained with similar environmental conditions to those on Mercury (e.g., Helbert et al., 2013). Nevertheless, the RELAB catalogue is characterised by its heterogeneity of measurements through different environmental and geometry conditions, and it provides general indications on mineralogy that may be present on the planet's surface.

To allow a direct comparison between the RELAB spectra and the measurements performed through the 11 MDIS-WAC filters, we rescaled laboratory spectra to camera filters (taking into consideration wavelength, bandwidth and transmission for each of the 11 MDIS-WAC filters used, see Supplementary Material Table 3; Hawkins et al., 2007).

An example of an original spectrum, Ti-rich pyroxene PYX126 (RELAB id. PP-EAC-061/C1PP61), and the resampled one are shown in Fig. 9.

4. Results

4.1. Geologic map

Classified as a C4 crater by Kinczyk et al. (2020) in a C1–C5 crater degradation scale (where C1 is the most degraded class, and C5 is the freshest), Lermontov crater has a broadly fresh rim. In fact, whereas in the western and northern parts the rim is identified by a sharp and still recognisable crest, but in the south-eastern border it is strongly reworked by post-impact modification processes, which in some cases make its identification difficult or not possible (Fig. 2).

Moreover, the boundary between proximal and distal ejecta deposits was hardly recognisable outside the crater, and therefore, all the ejecta deposits were classified as a single unit (Fig. 10).

The slopes within the crater wall exhibit a broadly rough morphology, identified in the geologic map as 'hummocky deposit' and relatable to the wall talus (Fig. 11). Within the crater wall, multiple sets of terraces are visible; these are more developed in the western part. These surfaces are usually delimited by steep scarps, whose margins were mapped when visible. As such, we interpreted the hummocky material as collapsed debris and reworked material due to mass wasting of surrounding scarps, and mapped this unit only within Lermontov crater, in order to differentiate it from a more pristine and smoother crater floor.

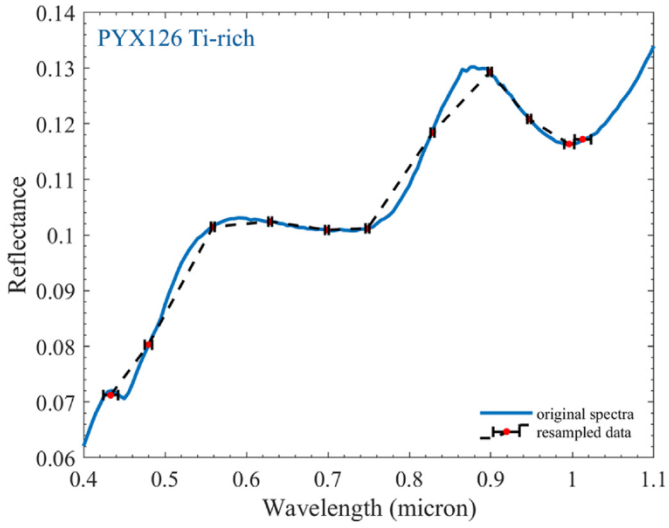

Fig. 9. Ti-rich pyroxene from Cloutis (2002), solid blue line, and the resampling result corresponding to the MDIS filters (red circle and black dashed line). The horizontal bars represent the MDIS-WAC filter bandwidths. (For interpretation of the references to colour in this figure legend, the reader is referred to the Web version of this article.)

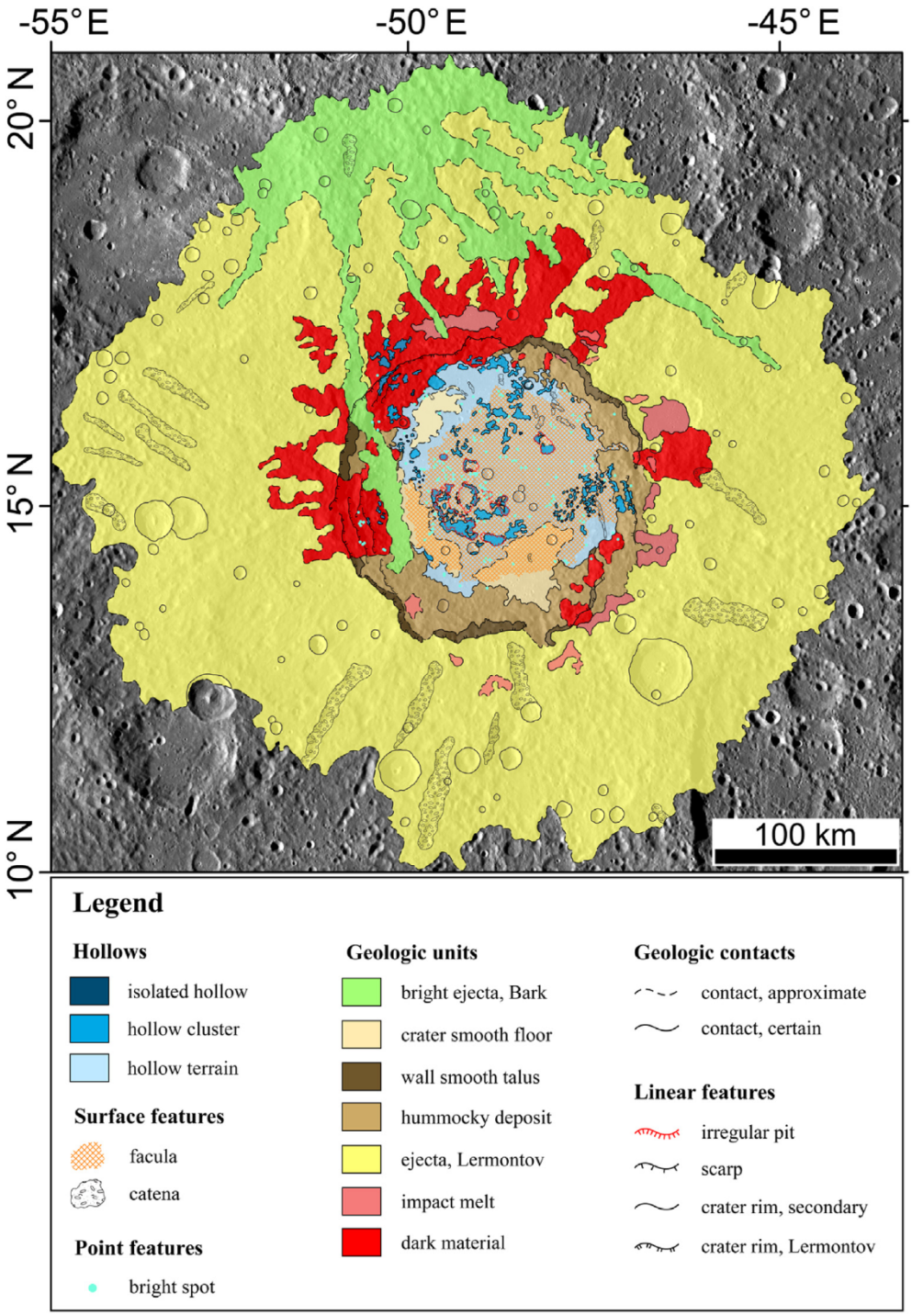

Fig. 10. The full Lermontov geological map (see text for details). The map projection is equidistant cylindrical with central meridian −48.9°E and central parallel 15.2°N. The planet radius is 2439.4 km.

Furthermore, very steep scarps are found close to the rim border, characterised by extremely smooth deposits distinguished from the rough, hummocky deposit previously described. This smoothness originates from surface 'polishing' caused by mass wasting processes during the final modification stage. These deposits were classified in the geologic map as 'wall smooth talus'.

We found no evidence of central uplift structures inside the crater. However, in the center of the crater floor, there are some small domes and crests that could be interpreted as remnants of an old central peak, but they were nonetheless reworked and modified by irregular pits and vents, from which pyroclastic deposits (described below) probably erupted. In addition, some smooth areas found either outside the crater, covering the ejecta deposits close to the rim, or within the hummocky deposit inside the crater are identified as melt pools related to the impact event of the Lermontov crater.

The crater floor appears strongly affected by hollow-related morphologies and deposits, which almost entirely cover the flat area inside the crater, and also some portions of the crater wall and ejecta (in the northern sector).

Hollows are mapped following the same classification adopted within Lucchetti et al. (2018), distinguishing 'isolated hollows', 'hollow clusters' and 'hollow terrain'. These units are characterised by, respectively, single

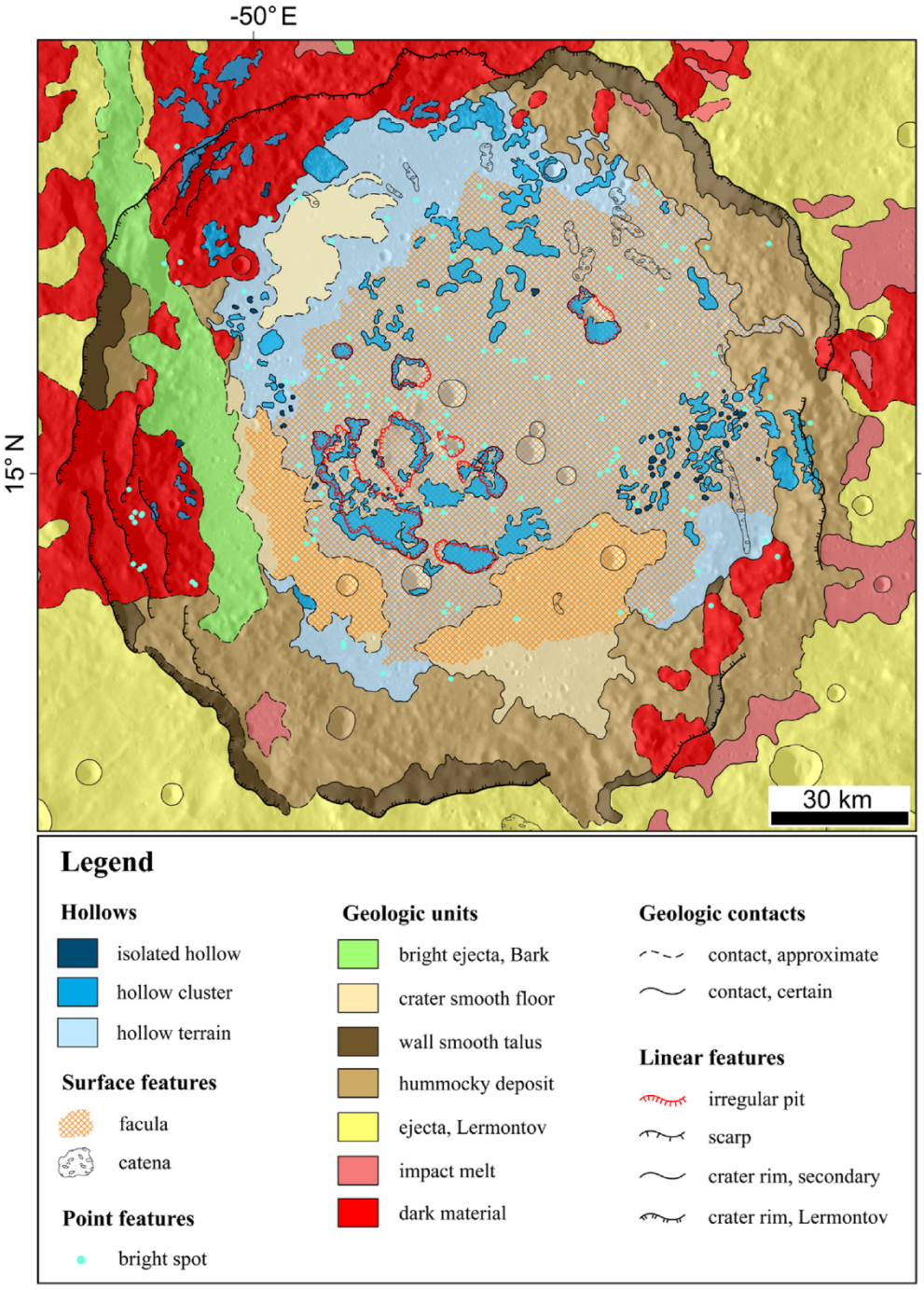

Fig. 11. A close up view of the geological map, focusing on the geologic units located in the inner part of Lermontov crater.

depressions that are at least 700-m large (at least 400–500 pixels when considering the NAC resolution of 26–48 m/pixel); wider depressions with irregular boundaries linked together, forming irregular sunken areas that range, in this area, from hundreds of metres up to tens of kilometres in width; high-albedo areas, with hollow-related morphologies, containing and surrounding scattered hollows that are too small to be individually mapped. In some cases, we used point features (i.e. 'bright spot' in the geologic map) to identify small, high-albedo features, which are probably associated with isolated hollows but too poorly resolved to be mapped as a superficial unit.

Moreover, analysing false-colour WAC images, in particular the MD3-colour, and the MDIS enhanced-colour (with the colour normalised Brovey sharpening technique applied) it was possible to recognise other superficial units, based on their spectral composition (different false colours are associated with different compositions of the material on the surface). The Lermontov crater, indeed, appears to be cross-cut by a bright ray of high-albedo material, which is attributed to the ejecta deposits of the Bark crater, located ~250 km north of Lermontov. These bright rays, mapped as a separate unit, cover part of the Lermontov ejecta deposits in the northern sector and cross-cut the crater itself in the western part, resulting in an easily distinguished stratigraphic marker, younger than the Lermontov impact event and its related geologic units. Furthermore, a substantial portion of the Lermontov ejecta deposits, along with some patches of hummocky deposits inside the crater, are characterised by a distinctive dark colour (dark blue in the MDIS false-colour images), which is probably associated with a low-reflectance

material component (Denevi et al., 2009) in the excavated material. Although in our study area the low-reflectance material is mainly identified as a colour signature and it is morphologically related to other geologic units (i.e. it is found within Lermontov ejecta, hummocky deposit and wall smooth talus), we nonetheless mapped this component as a separate geologic unit, named 'dark material', in order to better identify its signature within the geologic map.

Another important feature, identified within the crater floor, is an unnamed facula (i.e., a bright spot, usually attributed to pyroclastic deposits on Mercury; Kerber et al., 2011), which almost entirely covers the crater floor in the central and eastern portion, but it appears to be older than hollows deposits (which are found, therefore, on top of this facula). This *facula* is undetectable within the NAC images and not visible in the monochrome global basemaps, but its boundaries are obvious in the MDIS colour basemaps, and in particular in the enhanced-colour mosaic. All "colour" units have been mapped at an average scale of ~1:400 000.

4.2. Spectrophotometry and clustering

The four selected areas where we focused and applied the spectral clustering technique are presented in Fig. 8:

- Selection 1 is located in the south-west pyroclastic deposit and includes multiple irregular pits. By using the clustering technique, a natural number ("natural number" here refers to the number of clusters that are determined by the unsupervised classification) of eight clusters are identified (Fig. 12A). Each resulting cluster is characterised by its mean I/F and associated standard deviation. All spectra are then normalised at 0.56 μm to evaluate their mutual differences. Clusters numbered from 0 to 4 are typically associated with the pyroclastic deposit (with cluster no. 2 being the steepest/reddest one). Conversely, clusters numbered from 5 to 7 are associated with the bright rims of the pits (cluster no. 7 is the shallowest/bluest one);

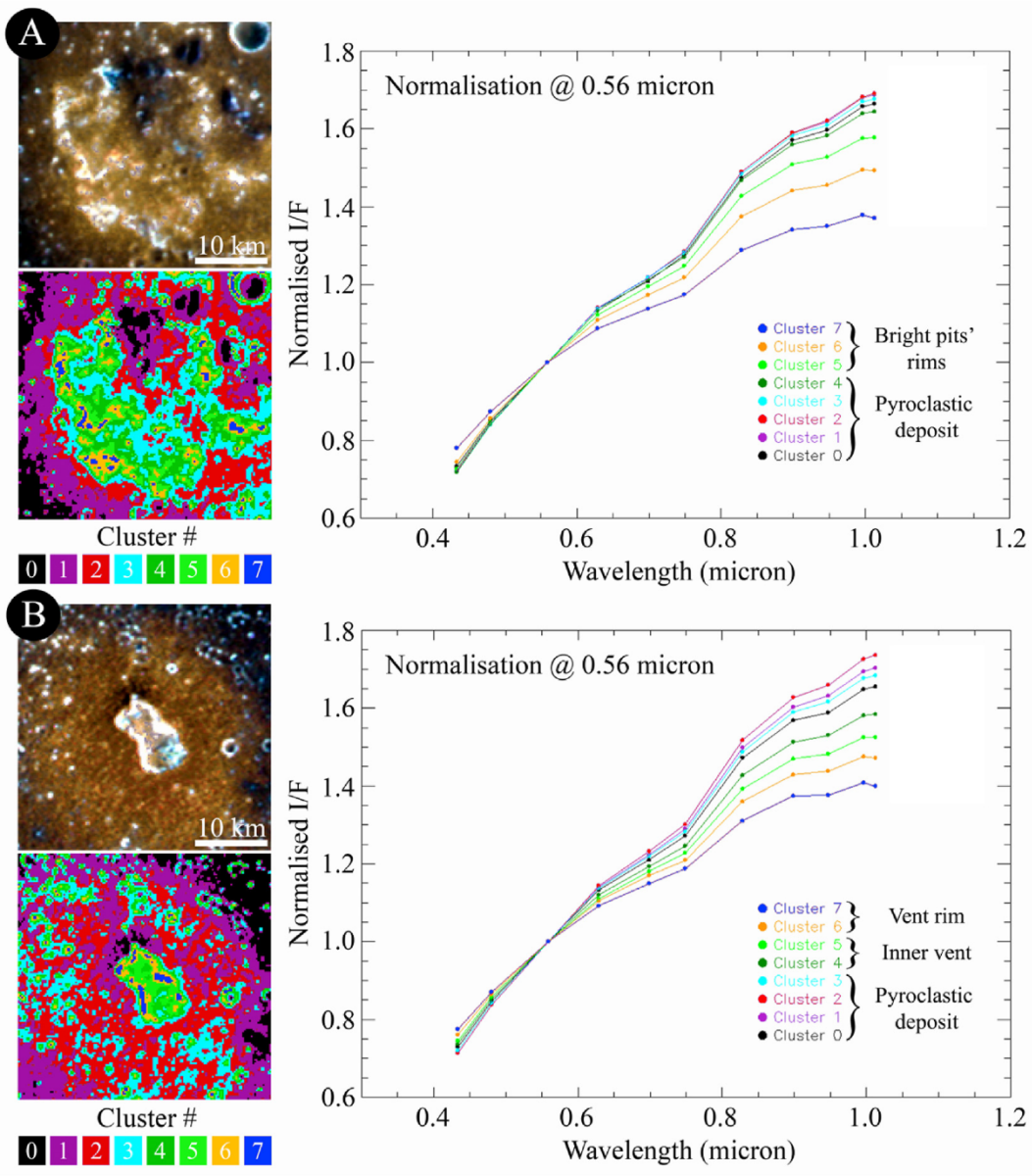

Fig. 12. A) Selection 1 (150 × 150 pixels) where we applied the clustering technique. The RGB image was prepared using the 1.012 μm filter for the red channel, the 0.698 μm filter for the green channel and the 0.433 μm filter for the blue channel (this configuration is used for all, following selections). The spectra obtained for all clusters are normalised at 0.56 μm). B) Selection 2 (150 × 150 pixels) returns 8 clusters as the natural number and it is centred on Lermontov NE vent. (For interpretation of the references to colour in this figure legend, the reader is referred to the Web version of this article.)

- Selection 2 covers the north-east Lermontov pyroclastic deposits and it includes the NE vent. Here eight clusters are identified (Fig. 12B). Clusters numbered 0 to 3 cover the red, pyroclastic deposit, with cluster no. 2 being the one with the reddest spectral behaviour, as well as covering the largest surface of the studied area. Instead, clusters no. 4 and 5 encompass the innermost part of the vent. Clusters 6 and 7 are almost entirely located in the vent's rim and show the shallowest trend (cluster no. 7 is the one presenting the bluest spectral trend among all spectra);
- Selection 3 lies on the hollow cluster area situated in the central-east part of Lermontov's floor (we hereafter call such hollows "field hollows"). 11 clusters are identified here (Fig. 13A). The clusters numbered from 0 to 3 are all located in the easternmost part of the selection, where hollows are sparse; clusters 4 and 5 cover the west-central part of the study area, where the red pyroclastic deposits occur. Cluster no. 5 is the one showing the steepest trend. Clusters 6 and 7 mostly surround the hollow clusters as well as isolated hollows, and show a flatter spectral behaviour than the previous clusters. Clusters from 8 to 10 are, instead, entirely located inside the hollows and present the bluest trend, with cluster 10 being the shallowest one;
- Selection 4 is located ~50 km from Lermontov's crater rim, inside the ejecta deposits. A natural number of eight clusters are identified, all presenting a similar (Fig. 13B) increase in reflectance as the wavelength increases from 0.4 to 1.05 μm. The shallowest cluster is no. 7, while the steepest one is no. 0.

5. Discussion

Estimate of the volatile concentrations driving the volcanic explosions:

The Lermontov crater floor is characterised by two pyroclastic deposits. Using both a stretched MDIS-WAC RGB image and a colour-normalised Brovey sharpening of the enhanced-colour basemap of the crater (Fig. 14A and B), we have been able to quantify the extents of the

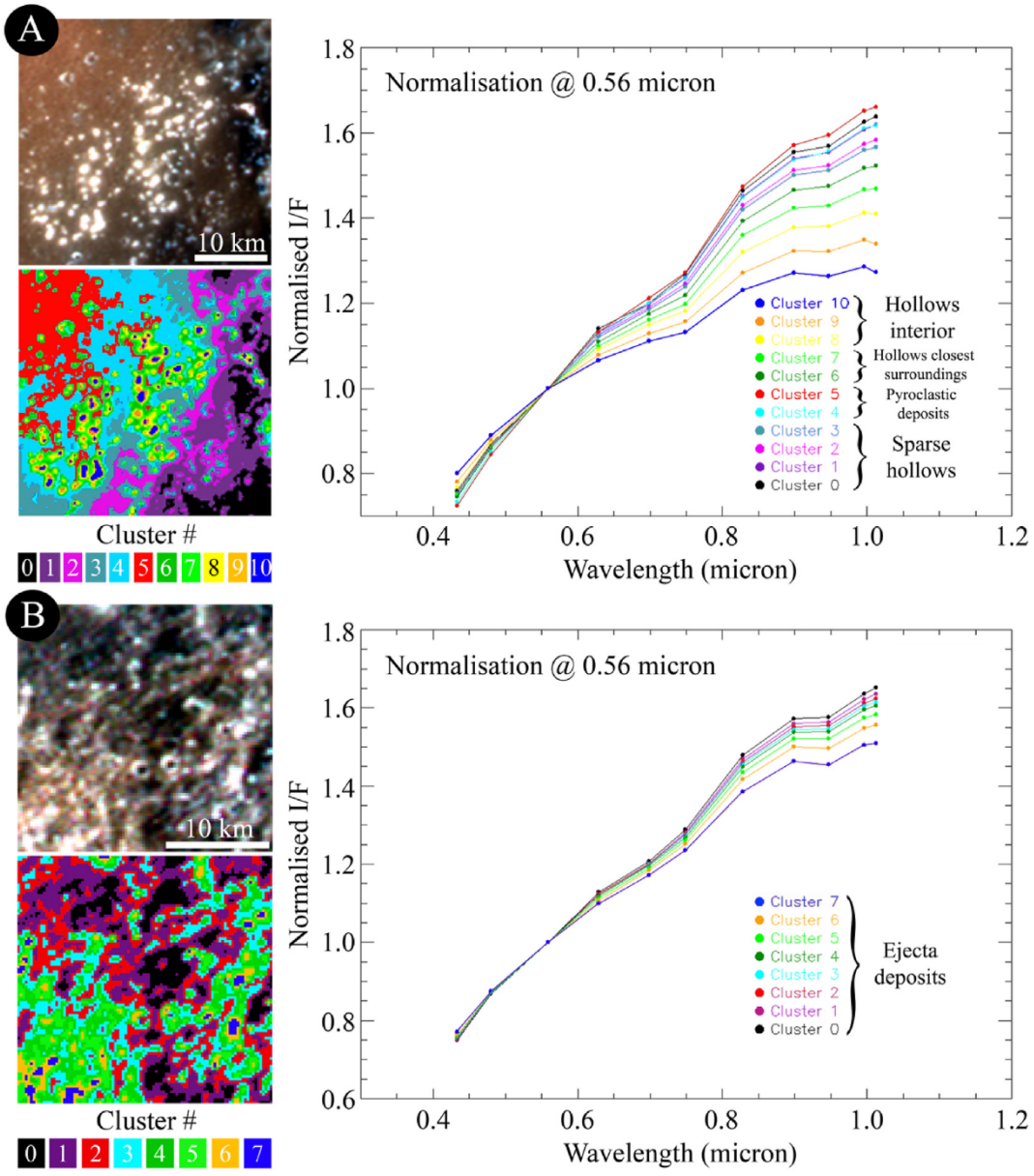

Fig. 13. A) Selection 3 (150 × 150 pixels) where we applied the clustering technique, together with the RGB image and the 11 identified clusters. The spectra obtained for all clusters are normalised at 0.56 μm). B) Selection 4 (100 × 100 pixels) returns 8 clusters as the natural number and it is located in the Lermontov ejecta deposits.

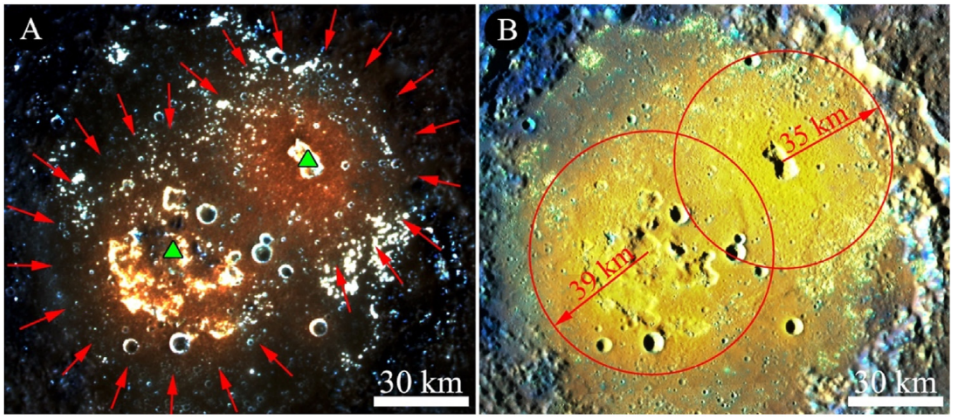

Fig. 14. A) Stretched RGB image, as in Fig. 1C, to highlight the extents of the two pyroclastic deposits (red arrows) identified on Lermontov floor. The two vents are indicated with the green triangles and are separated by 52 km. B) Colour Normalised Brovey Sharpening of the enhanced-colour basemap of Lermontov. The SW and NE pyroclastic deposits are highlighted with red circles, together with their ejecta ranges of 39 km and 35 km, respectively. (For interpretation of the references to colour in this figure legend, the reader is referred to the Web version of this article.)

two deposits, even if there is an uncertainty in the measurements based on MDIS WAC images (Besse et al., 2020). We derived an area of ~ 3800 km^2 for the NE deposit, and ~ 4800 km^2 for the SW deposit. This results in deposit radii ranging between 34 and 36 km for the NE deposit, and between 37 and 41 km for the SW one, comparable to other measured pyroclastic deposits on Mercury (Kerber et al., 2011). A previous analysis done on MESSENGER flybys 1–3 images (Kerber et al. (2011) suggested that the NE and SW deposits could be 33 and 31 km across, respectively. Recent measurements (Besse et al., 2020) reported new estimates of the NE and SW deposits extent of 40 and 45 km, which are based on MASCS (Mercury Atmospheric and Surface Composition Spectrometer; McClintock and Lankton 2007) spectral parameters analysis. Nonetheless, as the geological map (the facula in Fig. 11) and the red arrows of Fig. 14A highlight, the transition region between the red deposits and the surrounding units might be different from previous findings. If we assume a radius of 35 km for the NE deposit, and 39 km for the SW one and we insert them in Eq. 1 of Kerber et al. (2009), we can estimate the required vent eruption speed (v_e) as a function of the ejection angle (θ), to reach these maximum dispersal distances (Table 1).

Since during a hermean eruption there is no atmospheric drag dissipating its energy (Mercury is an airless body), the clasts ejected from the vent only interact with the volcanic gas entraining them (Wilson and Head, 1981). Such gas quickly decompresses to the point where gas-particle interactions become negligible, leaving the pyroclasts to follow ballistic trajectories back to the surface (Head and Wilson, 1979; Wilson and Keil, 1997; Kerber et al., 2011). For this reason, the maximum dispersal of pyroclasts takes place at θ equal to 45°, resulting in a minimum v_e (a smaller or larger ejection angle θ would need a greater v_e in order for the pyroclasts to reach the maximum dispersal distance; Table 1). By considering the gravitational acceleration at the surface of Mercury, g_{Merc}, of 3.7 m/s^2, we derive a minimum v_e of 360 m/s for the Lermontov NE deposit, and a minimum v_e of 380 m/s for the SW deposit.

In addition, Kerber et al. (2011) presented the required magmatic abundances (in parts per million; ppm) of different volatile species that would be needed to eject a pyroclastic particle to a specific distance of Mercury. We recall that the volatiles driving pyroclastic eruptions depend on the starting composition of the accreted planet, the redox state of the mantle, as well as the pressure and temperature conditions in effect while the erupting magma rises, hence affecting how the volatile components partition into the gas phase (Zolotov, 2011). The selected volatiles are those commonly encountered on Earth, such as carbon monoxide (CO), water vapour (H_2O), carbon dioxide (CO_2), sulfur dioxide (SO_2) and hydrogen sulfide (H_2S). However, since the reduced and dry conditions of Mercury's magmas imply gas speciation that is dissimilar to Earth's volcanic gases, Zolotov (2011) highlighted through chemical equilibrium models that nitrogen gas (N_2), CO, sulfide (S_2), carbon disulfide (CS_2), disulfur chloride (S_2Cl), chlorine (Cl), chlorine gas (Cl_2) and carbonyl sulfide (COS) may be among the most abundant volcanic gases of the planet (Zolotov (2011) suggested that species such as S, Cl and N could survive planetary devolatilisation events because they are stable in their solid, reduced forms.). Given that the identities of the volatiles triggering hermean pyroclastic explosions are still being debated, we decided to consider both Kerber et al. (2011) as well as Zolotov (2011) lists to estimate the magmatic abundances required to emplace pyroclastic material to the radial extent of the two Lermontov deposits (Table 2).

On Earth the amount of volcanic gases such as H_2S and SO_2 measured at the vent varies between 10^4 and 1.0–2.5 × 10^5 ppm, respectively, while for CS_2 or COS it may range between 1 and 100 ppm (Textor et al., 2003). For CO_2, this value can change between 10^4 and 4 × 10^5 ppm, while for water vapour it can be as high as 9 × 10^5. With the exception of H_2O (for Kilauea volcano in Hawaii a value of 3 × 10^3 ppm of H_2O has been measured; Gerlach, 1986), the amount of magmatic gases of Table 2 is comparable to (lower limits for CO_2, H_2S and SO_2), if not in excess of (CS_2 or COS), the quantity of volatiles detected at terrestrial vents. Therefore, regardless of the volatiles' mixtures that may have triggered the pyroclastic explosions inside Lermontov, this supports the

Table 1
The required vent eruption speeds v_e, computed in m/s at different angles of ejection θ (measured from the zenith) to reach Lermontov NE and SW maximum dispersal distances.

Deposit	Lermontov NE	Lermontov SW
Area (km^2)	~3800	~4800
Radius (km)	35	39
θ = 45° - Velocity (m/s)	360	380
θ = 30° - Velocity (m/s)	387	408
θ = 15° - Velocity (m/s)	509	537
θ = 7.5° - Velocity (m/s)	707	747

Table 2
Volatiles magmatic abundances in parts per million as from Kerber et al. (2011) and Zolotov (2011), computed to emplace pyroclastic material to the maximum radial extent of Lermontov NE and SW deposits.

Volatile	Lermontov NE	Lermontov SW
CO	8100	9000
H_2O	5200	5800
CO_2	12,700	14,100
SO_2	18,600	20,600
H_2S	9900	11,000
HCl	10,500	11,700
N_2	8100	9000
S_2	18,500	20,600
CS_2	22,000	24,500
S_2Cl	28,800	32,000
Cl	10,300	11,400
Cl_2	20,500	22,800
COS	17,400	19,300

interpretation of Kerber et al. (2009, 2011) and Asphaug and Reufer (2014) that the hermean interior has a higher than previously believed volatile content and it is not as extremely depleted in volatile materials as it was suggested by different models of volatile depletion (Boynton et al., 2007), such as disruption due to a giant impact (Wetherill, 1988; Benz et al., 1988, 2007) or vaporisation of the crust in the hot solar nebula (Fegley and Cameron, 1987).

From a spectral perspective, by applying the clustering technique to the Lermontov SW deposit (Sel. 1) and NE deposit (Sel. 2), we identified that clusters no. 2 of both selections are associated with the pyroclastic material situated in closest proximity to the vents. The comparison between the geological and the clustering map (Fig. 15A–D) reveals indeed that the reddest spectra are associated to the bright pyroclastic facula. Moreover, if we compare the two spectrophotometric behaviours (Fig. 15E) we note that they both overlap within the 1σ range, supporting the interpretation that the two pyroclastic deposits are spectrally similar. An alike surficial spectrophotometry may suggest that the two magmatic chambers supplying the vents have had a similar composition, despite their different sizes. An alternative hypothesis is that instead of two volatile reservoirs, there could be a single, bigger magma chamber that fed both vents, hence resulting in a similar ejected composition. This second possibility could be the most likely explanation given that the vents are only a short distance apart and are located within the same impact crater.

5.1. Vent topography

The high resolution DTM published by Fassett (2016) covers the central-northern part of the crater (Fig. 16A), and it returns an exhaustive representation of Lermontov NE vent and its closest surroundings with a spatial scale of 155 m and a vertical scale of few tens of m. The measured area of the vent is 81.2 km^2, with a length of ~12.5 km and a short axis spanning from 5 to 8 km. Such dimensions are comparable to other hermean vents (Table 1 of Kerber et al., 2011 shows length values ranging 7–38 km and widths spanning 4–28 km) but also to lunar vents resulting from explosive volcanic activity (Head et al., 2002). The maximum depth of the vent is instead ~ 0.95 km (Fig. 16B), which is shallower than the 1.2–2.4 km range obtained by Goudge et al. (2014) on six vents, but it is 0.15 km deeper than the Praxiteles crater vent (which has a comparable length of 13 km to the Lermontov one; Fassett, 2016).

Hollows are shallow pits that generally do not exceed depths of 50–100 m (Blewett et al., 2011, 2013). We highlight that the Fassett (2016) DTM used in this work presents a vertical accuracy value that is comparable to the hollows expected depths. For this reason, any observed depression shallower than 70–80 m and identified in Fig. 16B and C should be treated with caution. We tentatively extracted two profiles, I-II and III-IV to provide possible comparisons between the vent's depth and its closest surroundings, such as the hollow fields identified with bright patches in Fig. 16A. If confirmed (future DTMs characterised by higher spatial scale and better vertical accuracy will be prepared through the SIMBIO-SYS instrument dataset (Cremonese et al., 2020) in order to corroborate such depths or not), the identified depths highlight that hollows are "surficial" features that on Lermontov are 10–15 × shallower than the proximal NE vent.

Spectral interpretation and potential mineral candidates for the spectral absorptions observed:

Through the use of the MDIS-NAC high-resolution mosaics prepared for the geological mapping, we have identified hollows not only in the pyroclastic deposit located on the crater floor (field hollows), but also inside the SW and NE vents, particularly close to their rims (Fig. 17A–C for the SW vent, Fig. 17D for the NE vent).

Despite a 5 × to 10 × coarser spatial scale of the multiband WAC dataset with respect to the NAC one, the clustering technique is able to separate such "vent hollows" from their surrounding terrains, hence returning their spectral behaviour. Fig. 18A–D shows the presence of the vent rim hollows, which appear both in the geological close-up as well as in the clustering map. The hollows of the SW vent and those of the NE one are both characterised by a similar spectrum, within the 1σ range. If we then compare these hollows with the field ones (Sel. 3, Fig. 18E–G) we find that the vent hollows generally present a steeper spectral slope than the field hollows. This could be a consequence of their slightly different mineralogical composition, i.e. vent hollows may be mixed with some vent material (characterised by a steep spectral slope material).

In the past few years, two main hypotheses have been formulated to explain hollows formation (a recent, comprehensive study on this topic is presented in Wang et al., 2020): (1) hollows could be formed by a process

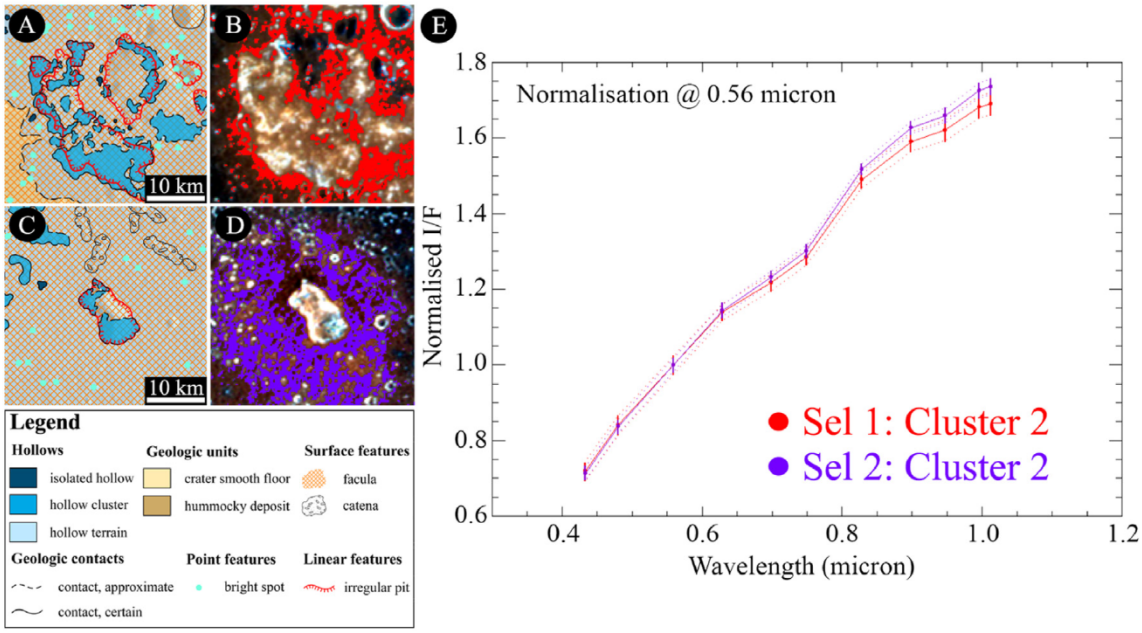

Fig. 15. A) Geological map closeup of Sel. 1. B) Clustering map on top of the RGB of Fig. 12A showing the extent of cluster no. 2. C) Geological map closeup of Sel. 2. D) Clustering map on top of the RGB of Fig. 12B showing the extent of cluster no. 2. E) Normalised I/F for the two clusters no. 2 extracted from Sel. 1 and 2. The vertical bars and the dotted lines show the 1σ range for each spectrum.

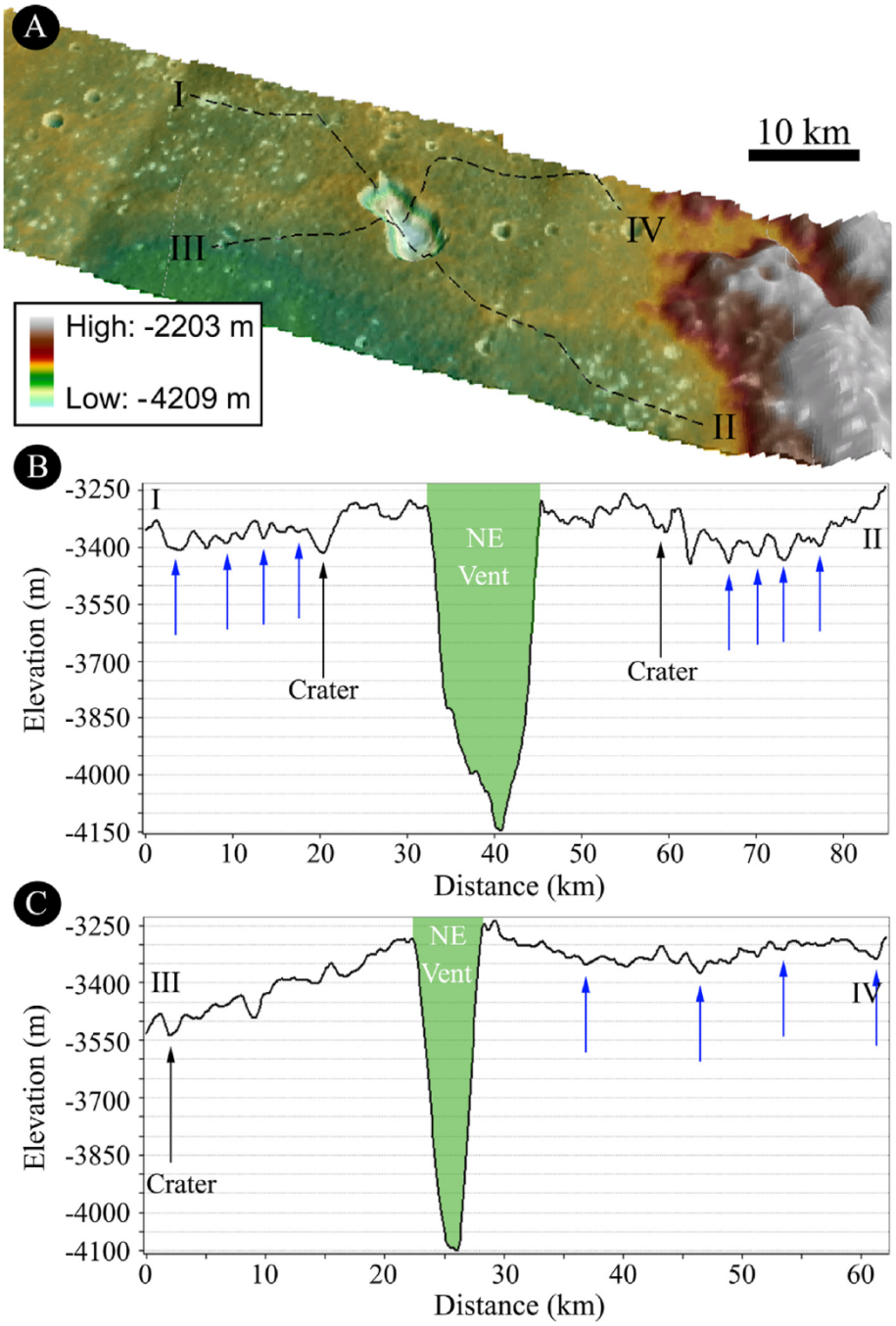

Fig. 16. A) 3D representation of the Lermontov NE vent and its closest surroundings. Elevation values are in m. Profiles I-II and III-IV are indicated on the DTM. B) Profile I-II showing the possible location of different hollows (blue arrows), craters (black arrows) and the Lermontov NE vent (longest dimension). C) Profile III-IV showing the location of possible different field hollows (blue arrows), craters (black arrows) and the Lermontov NE vent (shortest dimension). (For interpretation of the references to colour in this figure legend, the reader is referred to the Web version of this article.)

of "sublimation degradation" concerning the loss of one or more volatile phases that causes the remaining material to weaken and crumble, hence leading to ground collapse and lateral scarp retreat (Blewett et al., 2013); (2) hollows could be formed due to the loss of graphite from sputtering of carbon by space weathering and subsequent loss to space with brightening of material induced by the presence of dust (Blewett et al., 2016).

So far, Ca and Mg usually associated with Sulfur have been the most common elements cited to be constituents of volatile compounds (Blewett et al., 2011; Helbert et al., 2013). However, Murchie et al. (2015) argued that laboratory-measured reflectance values of MgS and CaS are too bright when compared to hollows. On the other hand, it is known from laboratory studies that smaller dust grain sizes are associated with an increasing reflectance in addition to a reddening of the spectrum (Cloutis et al., 2018), hence the hypothesis of graphite loss and brightening due to the presence of dust disagrees with the bluer spectra associated with hollows. It may be possible that this conundrum will be solved as a combination of the two hypotheses but new data such as those that will come from the BepiColombo mission (Benkhoff et al., 2010; Rothery et al., 2020) will be necessary to corroborate or deny the hypotheses mentioned so far.

Recently, Lucchetti et al. (2018) suggested that the presence of a mixture of different silicate minerals (sulfides and silicates with different relative abundances) may contribute to the absorptions found in their spectra. In particular, they proposed Ti-rich pyroxene, Cr-rich pyroxene and Ni-rich pyroxene as plausible end-members for hollows composition. Following this line of research, we selected multiple types of pyroxenes with enrichment of different elements. To exclude possible effects due to the peculiarities of the sample that could influence the matching process, we mediated all samples containing the same element (Cloutis, 2002). Therefore, PYX018, PYX153 and PYX170 (all catalogued as Cr-rich

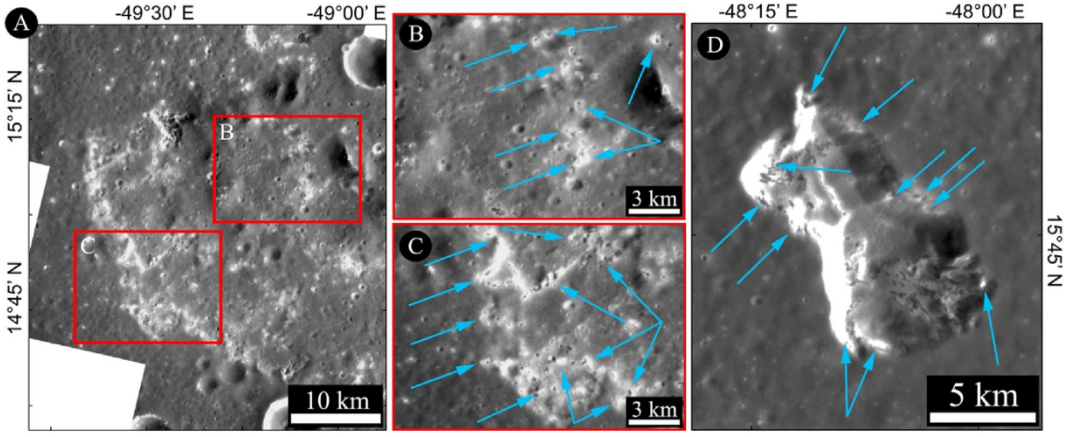

Fig. 17. A) High resolution mosaic showing the SW Lermontov vent. B) and C) are close-up views showing the presence of hollows (light blue arrows) inside the vent rims. D) High resolution mosaic showing the NE vent and the occurrence of hollows, indicated with light blue arrows. Note the different degradation states of the two vents (as previously highlighted by Goudge et al., 2014): the NE vents shows crisp edges, while the SW one has much more degraded edges. (For interpretation of the references to colour in this figure legend, the reader is referred to the Web version of this article.)

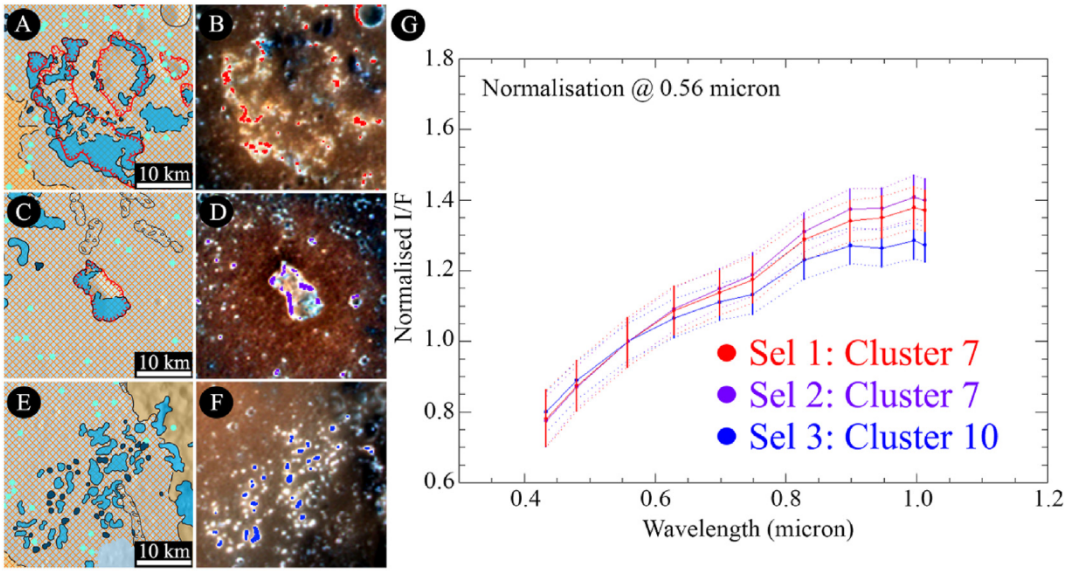

Fig. 18. A) Geological map closeup of Sel. 1. The legend is the same as Fig. 15. B) Clustering map on top of the RGB of Fig. 12A showing the extent of cluster no. 7. C) Geological map closeup of Sel. 2. D) Clustering map on top of the RGB of Fig. 12B showing the extent of cluster no. 7. E) Geological map closeup of Sel. 3. F) Clustering map on top of the RGB of Fig. 13A showing the extent of cluster no. 10. G) Normalised I/F for the two clusters no. 7 extracted from Sel. 1 and 2 and of cluster no. 10 extracted from Sel. 3. The vertical bars and the dotted lines show the 1σ range for each spectrum.

pyroxene) were averaged to obtain a representative spectrum of the class of mineral and the procedure has been repeated for Mn- and Ti-rich pyroxene. Original spectra from Cloutis (2002) and the average spectra evaluated in our work are reported in SM Fig. 1. In addition, following Lucchetti et al. (2018) we also selected Ni-rich pyroxene from White et al. (1971).

When focusing on the volatile compounds, Lucchetti et al. (2018) selected MgS, MnS and CaS, which are three thermally altered sulfides from Helbert et al. (2013). Since Zolotov (2011) suggested that chloride compounds may also be constituents of Mercury's mantle and magmas, we decided to add to our dataset three RELAB samples of MgCl (C1WV01) and CaCl (BKR1JBG29B).

In the four representative cluster spectra of Lermontov (Fig. 19) some spectral features are still recognisable, despite low spectral contrast. A broad band located between 0.63 μm and 0.83 μm seems to be present in all the spectra. A band at 0.95 μm clearly appears in the spectrum of the outer terrain cluster (this is the ejecta deposit mean spectrum of Sel. 4) and, with less spectral contrast, in the spectrum of both field and vent hollows. Hollow spectra seem to have a downturn at 1 μm that could be related to a broader spectral feature, but such feature cannot be identified or interpreted with MDIS-WAC data alone.

End-member spectra with a wide band between 0.6 μm and 0.8 μm are Ni-rich and Ti- rich pyroxene, as shown by Fig. 20A. On the contrary, sulfides and chloride have smaller bands that are not closely related to the broad band observed in the Lermontov spectra (Fig. 20B). For this reason, we can infer that the crater region might spectroscopically be dominated by the presence of a mix of various pyroxenes with different compositions and, in particular, those containing Ti and Ni. Conversely, the hint of a band at 0.95 μm is not typical of pyroxene, which is usually characterised by a broader band around 1 μm.

When focusing on the pyroclastic deposit and the outer terrain, the differences between them are observed in the wavelength range 0.55–0.75 μm. The outer terrain minimum peak is located at 0.69 μm while the pyroclastic deposit maximum absorption is shifted towards

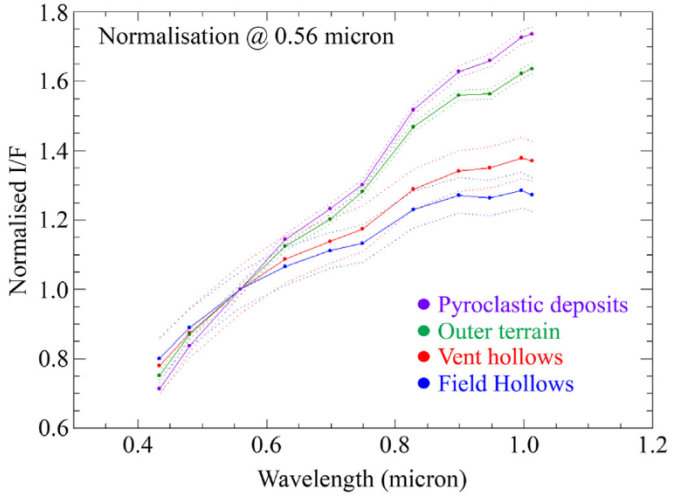

Fig. 19. The representative cluster spectra of Lermontov are taken from Fig. 15E (pyroclastic deposits), Fig. 18G (vent hollows and field hollows) and Fig. 13B (outer terrain).

0.75 μm. By looking at Fig. 20A, this difference could be interpreted as a possible difference in mineralogy with a pyroclastic deposit composition linked with Ni- and Ti-rich pyroxene, while the outer terrain might be dominated by Cr-, and possibly, Mn-rich pyroxene. Moreover, the differences between the pyroclastic spectrum and the outer terrain spectrum around 0.55–0.62 μm could be linked with both the presence/absence of MnS and MgS. Indeed, as shown in Fig. 20B, these compounds are characterised by bands localised in this spectral region, as is Mn-rich pyroxene (Fig. 20A). Although MgCl and CaCl (Fig. 20B) do not have spectral features in this region, they are suggested as possible hermean volcanic gases too (Zolotov, 2011), therefore, we cannot exclude their presence, with their flatter spectral slope that could be responsible for the blueing observed in hollows spectra. Moreover, CaCl spectrum shows a slight downturn at 1 μm that could be responsible for the observed downturn in hollows.

Instead, if we compare the field hollows to the pyroclastic and the outer terrain spectra, hollows seem to be systematically less intense in the wavelength range 0.48–0.82 μm. The band at 0.55 μm could be related to CaS and the differences at 0.48 μm and 0.62 μm could be related to other volatiles compounds such as MgS. This supports the interpretation that field hollows are less rich in such volatile elements compared with the pyroclastic material. Moreover, the maximum absorption peak of the hollows' spectrum is localised at 0.82 μm, as with the pyroclastic spectra: this is possibly linked to the presence of Ti-rich pyroxene.

The similarity in spectral profile between pyroclastic and vent hollows, coupled with the slope differences showing a redder spectrum for vent hollows and a bluer spectrum for field hollows, confirms that vent hollows are mixed with some vent material, while field hollows are not. This supports the interpretation that hollows' formation mechanism is unable to completely overwrite the spectral signature of the surrounding terrain, and their spectroscopic appearance is mixed with the composition of the terrain where they form, with the result of a mixed behaviour between the two components (Lucchetti et al., 2018).

Finally, by comparing the Lermontov hollows spectra to the ones previously obtained from completely different geological settings (Vilas et al., 2016; Lucchetti et al., 2018), we can see that their spectral slope is generally redder/steeper (Fig. 21). This difference is not surprising given that their origin is deeply rooted to the pyroclastic activity itself.

Velasquez and Lermontov hollows present similar spectra but hollows in Lermontov have a more pronounced 0.95 μm absorption feature. The Dominici hollows are the most different ones with two very broad bands in the 0.6–0.8 μm range and above 0.9 μm. Canova hollows, instead, are

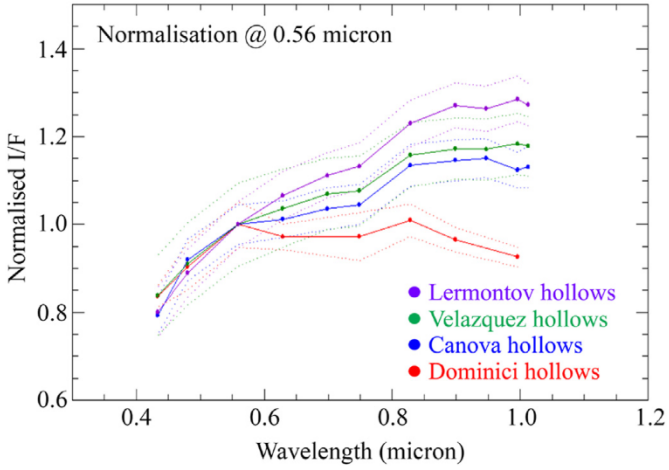

Fig. 21. Comparison between the spectral behaviour of Lermontov hollows and those analysed in the Velazquez, Canova, and Dominici craters (Lucchetti et al., 2018; Vilas et al., 2016).

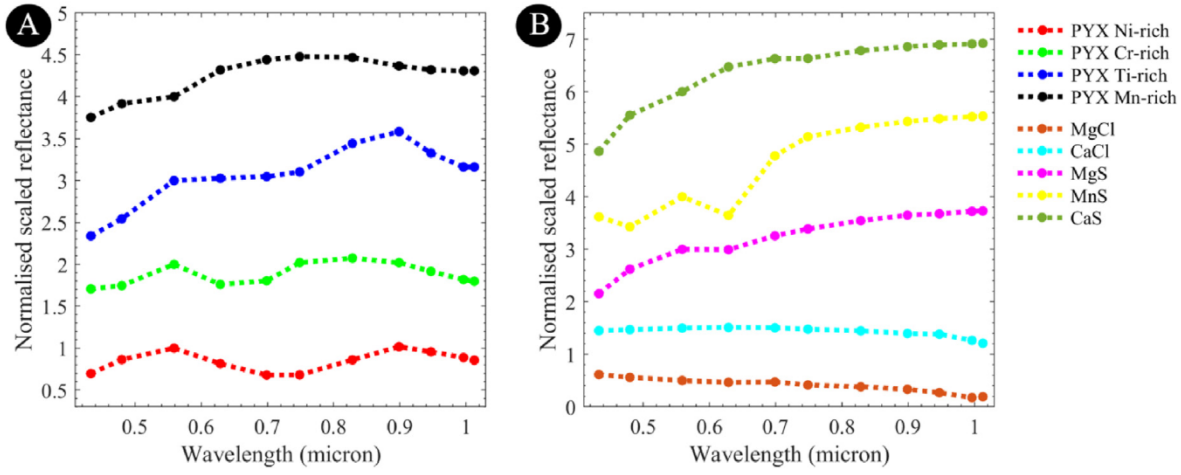

Fig. 20. A) MDIS-WAC resampled Ti-rich, Mn-rich and Cr-rich pyroxene spectra from Cloutis (2002) and Ni-rich pyroxene spectra from White et al. (1971). Spectra are normalised at 0.56 μm but shifted for clarity. B) MDIS-WAC resampled spectra of MgS, MnS and CaS sulfides after thermal alteration from Herbert et al. (2013) along with chloride spectra from RELAB: MgCl (WV-JWH-001/C1WV01) and CaCl (JB-JLB-G29-B/BKR1JBG29B). Spectra are normalised at 0.56 μm but shifted for clarity.

intermediate between the Dominici hollows and those of Velasquez and Lermontov. Moreover, the hollows at Canova crater show a possible shoulder at 0.62 μm and a small absorption at 0.99 μm, not observed in Lermontov. It appears that differences between hollows spectra can be due to a wide range of variables, such as compound abundances, grain size and/or age (Vilas et al., 2016).

We recall that these findings must consider the limitation of the MDIS WAC calibration reported in Denevi et al. (2018b), hence suggesting caution in interpreting features in MDIS spectra found in individual WAC data sets.

6. Conclusions

Using both monochromatic MESSENGER MDIS-NAC and multiband MDIS-WAC images we performed a multidisciplinary analysis of Lermontov crater on Mercury, a 166 km diameter crater where red pyroclastic deposits and bright blue hollows and haloes coexist. We prepared the first high-resolution geological map of the Lermontov floor and its closest surroundings, identifying eight different geologic units and an unnamed bright facula, which almost covers the crater floor in the central and eastern portion.

A detailed analysis of the two pyroclastic deposits of Lermontov returned radii ranging between 34 and 36 km (the NE one) and 37–41 km (the SW one), comparable to other measured pyroclastic deposit radii on Mercury. Such deposits are centred on two vents: i) the NE vent has crisp edges, a depth of 0.95 km and when it erupted, its pyroclasts were ejected at a minimum speed of 360 m/s; ii) on the contrary the Lermontov SW vent has much more degraded edges and it likely erupted with a minimum velocity of 380 m/s. Despite a vent physical separation of 52 km, the pyroclastic material located in close proximity to both vents has a similar spectrophotometric behaviour. This suggests that the two magmatic chambers that supplied the eruptions might have had a similar chemical composition. An alternative hypothesis is that instead of two volatile reservoirs, there could be a single magmatic chamber that may have fed both vents, hence resulting in a similar ejected composition.

The magmatic volatile abundances that could have driven the Lermontov explosions are comparable to, if not in excess of, the quantity of volatiles detected at terrestrial vents. This supports the interpretation that the hermean interior is not as extremely depleted in volatile material as it was suggested in the past scientific literature.

The pyroclastic deposits located on Lermontov's floor have a steep, red spectral behaviour dominated by the presence of a mixture of various Ni-rich and Ti-rich pyroxenes. Conversely, the vents' rims are characterised by several hollows whose spectral slope is bluer that the pyroclastic deposits themselves. When comparing the vent hollows to the field ones located farther out, the former have a spectral trend in the 0.62–0.82 μm range that is more similar to the pyroclastic spectrum. The hollows' band located at 0.55 μm could be related to CaS while the small differences at 0.48 μm and 0.62 μm could be due to the presence of other volatiles compounds, such as MgS. Similar, but less intense absorptions vent hollows and pyroclastic deposits have in common suggest that: i) the hollows' formation mechanism, and hence their spectroscopic appearance, is not disconnected from the composition of the terrain where they formed, and that ii) vent hollows are less rich in such volatile elements when compared with the pyroclastic deposits.

Overall, Lermontov hollows are characterised by steeper spectra with respect to the ones located in other different hermean geological settings. This supports the interpretation that hollows' formation mechanism does not completely overwrite the spectral signature of the surrounding terrain, and their spectroscopic appearance is mixed with the composition of the terrain where they form.

Hollows and vent deposits are important sources of information about planetary structure and composition. In particular, the coexistence of pyroclastic deposits, vents and field hollows inside the studied crater provides hints about Mercury's past and present volatile budget. Lermontov crater will therefore be target of interest for the future ESA/JAXA BepiColombo mission (Benkhoff et al., 2010) and a set of dedicated observations focusing on its vents, pyroclastic deposits and hollows will be granted through the STC, HRIC and VIHI instruments of the SIMBIO-SYS suite (Cremonese et al., 2020).

CRediT author statement

Maurizio Pajola: Conceptualization, Methodology, Software, Investigation, Visualization, Formal analysis, Writing - original draft, Writing - review & editing. **Alice Lucchetti**: Methodology, Investigation, Visualization, Formal Analysis, Software, Writing - Review & Editing. **Andrea Semenzato**: Methodology, Investigation, Visualization, Formal Analysis, Writing - Review & Editing. **Giovanni Poggiali**: Methodology, Investigation, Visualization, Formal Analysis, Writing - Review & Editing. **Giovanni Munaretto**: Investigation, Writing - Review & Editing. **Valentina Galluzzi**: Methodology, Writing - Review & Editing. **Giuseppe A. Marzo**: Software, Writing - Review & Editing. **Gabriele Cremonese**: Writing - Review & Editing, Funding Acquisition. **John R. Brucato**: Methodology, Writing - Review & Editing. **Pasquale Palumbo**: Writing - Review & Editing. **Matteo Massironi**: Writing - Review & Editing, Funding Acquisition.

Declaration of competing interest

The authors declare that they have no known competing financial interests or personal relationships that could have appeared to influence the work reported in this paper.

Acknowledgments

We thank Dr. Zhiyong Xiao and an anonymous referee for important and constructive comments that lead to a substantial improvement of the paper. This research has been realised under the BepiColombo ASI-INAF contract no 2017- 47-H.0. This manuscript is part of a project that has received funding from the European Union's Horizon 2020 research and innovation programme under grant agreement N°776276 (PLANMAP). The NASA PDS Cartography and Imaging Science Node, as well as the USGS Astrogeology Science Center PILOT Node are acknowledged for providing access to the MDIS dataset used in this work. This research utilises spectra downloaded by NASA RELAB facility at Brown University. This work is dedicated to all doctors who gave and are still giving their energy, time and lives during the ongoing COVID-19 pandemic and to Arja, who sadly left us well ahead of time.

Appendix A. Supplementary data

Supplementary data to this article can be found online at https://doi.org/10.1016/j.pss.2020.105136.

Data availability

The data used in this manuscript can be found at the NASA PDS Cartography and Imaging Science Node, as well as at the USGS Astrogeology Science Center PILOT Node.

References

Asphaug, E., Reufer, A., 2014. Mercury and other iron-rich planetary bodies as relics of inefficient accretion. Nat. Geosci. 7, 564–568.
Becker, K.J., et al., 2016. First global digital elevation model of Mercury. In: Paper Presented at the 47th Lunar and Planetary Science Conference. Lunar and Planetary Institute, Houston, TX. Astract no. 2959.
Benkhoff, J., et al., 2010. BepiColombo-Comprehensive exploration of Mercury: mission overview and science goals. Planet. Space Sci. 58, 2–20.
Benz, W., et al., 1988. Collisional stripping of Mercury's mantle. Icarus 74, 516–528.
Benz, W., et al., 2007. The origin of Mercury. Space Sci. Rev. 132, 189–202.

Besse, S., et al., 2020. Spectral properties and physical extent of pyroclastic deposits on Mercury: variability within selected deposits and implications for explosive volcanism. J. Geophys. Res.: Plan 125 (5), e2018JE005879.
Blewett, D.T., et al., 2009. Multispectral images of Mercury from the first MESSENGER flyby: analysis of global and regional color trends. Earth Planet Sci. Lett. 285, 263–271.
Blewett, D.T., et al., 2011. Hollows on Mercury: MESSENGER evidence for geologically recent volatile-related activity. Science 333 (6051), 1856–1859. https://doi.org/10.1126/science.1211681.
Blewett, D.T., et al., 2013. Mercury's hollows: constraints on formation and composition from analysis of geological setting and spectral reflectance. J. Geophys. Res. Planets 118. https://doi.org/10.1029/2012JE004174.
Blewett, D.T., et al., 2016. Analysis of MESSENGER high-resolution images of Mercury's hollows and implications for hollow formation. J. Geophys. Res.: Plan 121, 1798–1813.
Boynton, W.V., et al., 2007. MESSENGER and the chemistry of Mercury's surface. Space Sci. Rev. 131, 85–104.
Calinski, T., Harabasz, J., 1974. A dendrite method for cluster analysis. Commun. Stat. 3, 1–27.
Cloutis, E.A., 2002. Pyroxene reflectance spectra: minor absorption bands and effects of elemental sustitutions. J. Geophys. Res. 107 (E6), 5039. https://doi.org/10.1029/2001JE001590.
Cloutis, E.A., et al., 2018. Spectral reflectance "deconstruction" of the Murchison CM2 carbonaceous chondrite and implications for spectroscopic investigations of dark asteroids. Icarus 305, 203–224.
Cremonese, G., et al., 2020. SIMBIO-SYS: scientific cameras and spectrometer for the BepiColombo mission. Space Sci. Rev. 216, 75.
Dalle Ore, C., et al., 2012. Infrared spectroscopic characterization of the low-albedo materials on Iapetus. Icarus 221 (2), 735.
Dalle Ore, C.M., et al., 2018. Ices on Charon: distribution of H_2O and NH_3 from new horizons LEISA observations. Icarus 300, 21.
Davies, M.E., Dornik, S.E., Gault, D.E., Strom, R.G., 1978. Atlas of Mercury. NASA Special Publication, p. 423.
DeHon, R.A., et al., 1981. Geologic map of the kuiper (H6) quadrangle of Mercury. U.S. Geol. Surv. Misc. Invest. Ser. Map I–1233.
Denevi, B.W., et al., 2009. The evolution of Mercury's crust: a global perspective from MESSENGER. Science 324 (5927), 613–618.
Denevi, B.W., et al., 2018a. The geologic history of Mercury. In: Mercury, the View after MESSENGER. Cambridge University Press. https://doi.org/10.1017/9781316650684.
Denevi, B.W., et al., 2018b. Calibration, projection, and final image products of MESSENGER's Mercury Dual Imaging System. Space Sci. Rev. 214 (2).
Domingue, D.L., et al., 2015. Mercury's global color mosaic: an update from MESSENGER's orbital observations. Icarus 257, 477–488. https://doi.org/10.1016/j.icarus.2014.11.027.
Du, Q., et al., 2007. On the performance evaluation of pan-sharpening techniques. Geosci. Rem. Sens. Lett. IEEE 4 (4), 518–522.
Dzurisin, D., 1977. Mercurian bright patches: evidence for physio-chemical alteration of surface material? Geophys. Res. Lett. 4 (10), 383–386.
Fasset, C.I., 2016. Ames stereo pipeline-derived digital terrain models of Mercury from MESSENGER stereo imaging. Planet. Space Sci. 134, 19–28.
Fegley, B., Cameron, A.G.W., 1987. A vaporization model for Fe/Si fractionation in the Mercury protoplanet. Earth Planet Sci. Lett. 82, 207–222.
Fonti, S., Marzo, G.A., 2010. Mapping the methane on Mars. Astron. Astrophys. 512 (A51), 6.
Gaddis, L.R., et al., 2003. Compositional analyses of lunar pyroclastic deposits. Icarus 161, 262–280.
Gerlach, T.M., 1986. Exsolution of H_2O, CO_2, and S during eruptive episodes at Kilauea volcano, Hawaii. J. Geophys. Res. 91, 12177–12185.
Goudge, T.A., et al., 2014. Global inventory and characterization of pyroclastic deposits on Mercury: new insights into pyroclastic activity from MESSENGER orbital data. J. Geophys. Res. Planets 119, 635–658. https://doi.org/10.1002/2013JE004480.
Hawkins, S.E., et al., 2007. The Mercury dual imaging System on the MESSENGER spacecraft. Space Sci. Rev. 131 (1–4), 247–338.
Head, J.W., Wilson, L., 1979. Alphonsus-type dark-halo craters: morphology, morphometry and eruption conditions. Proc. Lunar Planet Sci. Conf. 10, 2861–2897.
Head, J.W., et al., 2002. Dark ring in southwestern Orientale basin: origin as a single pyroclastic eruption. J. Geophys. Res. 107 (E1), 5001. https://doi.org/10.1029/2000JE001438.
Helbert, J., et al., 2013. Visible and near-infrared reflectance spectra of thermally processed synthetic sulfides as a potential analog for the hollow forming materials on Mercury. Earth Planet Sci. Lett. 369–370, 233–238.
Izenberg, N.R., et al., 2014. The low-iron, reduced surface of Mercury as seen in spectral reflectance by MESSENGER. Icarus 228, 364–374.
Kerber, L., et al., 2009. Explosive volcanic eruptions on Mercury: eruption conditions, magma volatile content, and implications for interior volatile abundances. Earth Planet Sci. Lett. 285, 263–271.
Kerber, L., et al., 2011. The global distribution of pyroclastic deposits on Mercury: the view from MESSENGER flybys 1-3, Planet. Space Sci 59, 1895–1909.
Kinczyk, M.J., Prockter, L.M., Byrne, P.K., Susorney, H.C., Chapman, C.R., 2020. A morphological evaluation of crater degradation on Mercury: revisiting crater classification with MESSENGER data. Icarus 341, 113637.
Lucchetti, A., et al., 2018. Mercury hollows as remnants of original bedrock materials and devolatilization processes: a spectral clustering and geomorphological analysis. J. Geophys. Res.: Plan 123. https://doi.org/10.1029/2018JE005722.
Lucchitta, B.K., Schmitt, H.H., 1974. Orange material in the Sulpicius Gallus formation at the southwestern edge of mare serenitatis. Proc. Lunar. Sci. Conf. 5, 223–234.
Marzo, G.A., et al., 2006. Cluster analysis of planetary remote sensing spectral data. J. Geophys. Res. 111, E03002. https://doi.org/10.1029/2005JE002532.
Marzo, G.A., et al., 2008. Statistical exploration and volume reduction of planetary remote sensing spectral data. J. Geophys. Res. 113, E12009. https://doi.org/10.1029/2008JE003219.
Marzo, G.A., et al., 2009. Automated classification of visible and infrared spectra using cluster analysis. J. Geophys. Res. 114, E08001. https://doi.org/10.1029/2008JE003250.
McClintock, W.E., Lankton, M.R., 2007. The Mercury atmospheric and surface composition spectrometer for the MESSENGER mission. Space Sci. Rev. 131 (1–4), 481–521.
Murchie, S.L., et al., 2015. Orbital multispectral mapping of Mercury with the MESSENGER Mercury Dual Imaging System: evidence for the origins of plains units and low-reflectance material. Icarus 254, 287–305.
Pajola, M., et al., 2018. Phobos MRO/CRISM visible and near-infrared (0.5-2.5 micron) spectral modeling. Planet. Space Sci. 154, 63–71.
Parente, C., Pepe, M., 2017. Influence of the weights in IHS and Brovey methods for pan-sharpening WorldView-3 satellite images. Int. J. Eng. Technol. 6 (3), 71–77.
Pinilla-Alonso, N., et al., 2011. Iapetus surface variability revealed from statistical clustering of a VIMS mosaic: the distribution of CO2. Icarus 215 (1), 75.
Rava, B., Hapke, B., 1987. An analysis of the Mariner 10 color ratio map of Mercury. Icarus 71, 397–429.
Robinson, M.S., et al., 2008. Reflectance and color variations on Mercury: regolith processes and compositional heterogeneity. Science 321, 66–69.
Rothery, D.A., et al., 2020. Rationale for BepiColombo studies of Mercury's surface and composition. Space Sci. Rev. 216, 66.
Schultz, P.H., 1977. Endogenic modification of impact craters on Mercury. Phys. Earth Planet. In. 15, 202–219.
Solomon, S.C., et al., 2007. MESSENGER mission overview. Space Sci. Rev. 131 (1–4), 3–39. https://doi.org/10.1007/s11214-007-9247-6.
Textor, C., et al., 2003. Emissions from volcanoes. In: Granier, Claire, Reeves, Claire, Artaxo, Paulo (Eds.), Emissions of Chemical Compounds and Aerosols in the Atmosphere. Kluwer, Dordrecht.
Thomas, R.J., et al., 2014. Long-lived explosive volcanism on Mercury. Geophys. Res. Lett. 41 (17), 6084–6092.
Vilas, F., et al., 2016. Mineralogical indicators of Mercury's hollows composition in MESSENGER color observations. Geophys. Res. Lett. 43, 1450–1456.
Wang, Y., et al., 2020. Lost volatiles during the formation of hollows on Mercury. J. Geophys. Res.: Plan 125, e2020JE006559. https://doi.org/10.1029/2020JE006559.
Wetherill, G.W., 1988. Accumulation of Mercury from planetesimals. In: Vilas, F., Chapman, C.R., Matthews, M.S. (Eds.), Mercury. University of Arizona Press, Tucson, AZ, pp. 670–691.
White, W.B., et al., 1971. Optical spectra of chromium, nickel, and cobalt-containing pyroxenes. American Mineralogist. Journal of Earth and Planetary Materials 56 (1–2), 72–89.
Wilson, L., Head, J.W., 1981. Ascent and eruption of basaltic magma on the Earth and Moon. J. Geophys. Res. 86, 2971–3001.
Wilson, L., Keil, K., 1997. The fate of pyroclasts produced in explosive eruptions on the asteroid 4 Vesta. Meteoritics Planet Sci. 32, 813–823.
Zolotov, M. Yu, 2011. On the chemistry of mantle and magmatic volatiles on Mercury. Icarus 212, 24–41. https://doi.org/10.1016/j.icarus.2010.12.014.